

Two points are enough

Hao Liu^{*†a}, Yanbin Zhao^{*†a}, Huarong Zheng^b, Xiulin Fan^c, Zhihua Deng^d, Mengchi Chen^e, Xingkai Wang^f, Zhiyang Liu^e, Jianguo Lu^c, Jian Chen^{*g}

^aState Key Laboratory of Fluid Power Components and Mechatronic Systems, School of Mechanical Engineering, Zhejiang University, Hangzhou, China

^bOcean College, Zhejiang University, Hangzhou, China

^cState Key Laboratory of Silicon and Advanced Semiconductor Materials, School of Materials Science and Engineering, Zhejiang University, Hangzhou, China

^dEnergy Research Institute at NTU (ERI@N), Nanyang Technological University, Singapore

^eSchool of Control Science and Engineering, Zhejiang University, Hangzhou, China

^fSchool of Materials Science and Engineering, Tianjin University, Tianjin, China

^gSchool of System Design and Intelligent Manufacturing, Southern University of Science and Technology, Shenzhen, China

Abstract

Prognosis and diagnosis play an important role in accelerating the development of lithium-ion batteries, as well as reliable and long-life operation. In this work, we answer an important question: What is the minimum amount of data required to extract features for accurate battery prognosis and diagnosis? Based on the first principle, we successfully extracted the best two-point feature (BTPF) for accurate battery prognosis and diagnosis using the fewest data points (only two) and the simplest feature selection method (Pearson correlation coefficient). The BTPF extraction method is tested on 820 cells from 6 open-source datasets (covering five different chemistry types, seven manufacturers, and three data types). It achieves comparable accuracy to state-of-the-art features in both prognosis and diagnosis tasks. This work challenges the cognition of existing studies on the difficulty of battery prognosis and diagnosis tasks, subverts the fixed pattern of establishing prognosis and diagnosis methods for complex dynamic systems through deliberate feature engineering, highlights the promise of data-driven methods for field battery prognosis and diagnosis applications, and provides a new benchmark for future studies.

Keywords:

^{*†} These authors contributed equally to this work: Hao Liu, Yanbin Zhao.

^{*}Corresponding author

Email addresses: haoliu7850052@zju.edu.cn (Hao Liu^{*†}), zyb9825@zju.edu.cn (Yanbin Zhao^{*†}), chenjj8@sustech.edu.cn (Jian Chen^{*})

Lithium-ion battery, feature engineering, prognosis, diagnosis, first principle, remaining useful life, state of health, machine learning.

1. Introduction

Lithium-ion (Li-ion) batteries have been commercialized on a large scale in portable electronic products, transportation cars, and stationary energy storage systems. These fields urgently need batteries with lower cost [1, 2], higher energy density [3, 4], shorter fast-charging time [5], longer cycle life [6, 7], and better safety [8]. Prognosis [9] and diagnosis [10] are vital for battery optimization. Prognosis can be utilized to accelerate the optimization of battery design [11], production [12], and management [13], thereby saving a lot of time and economic costs. Diagnosis can be utilized to monitor the state of health (SoH), optimize management strategies, and perform reliable maintenance, thereby reducing the occurrence of safety incidents and extending the battery life [14, 15, 16]. Recently, thanks to the open-source of many battery test datasets [17], researchers have proposed many data-driven methods that combine machine learning (ML) and feature engineering to achieve high-precision battery prognosis and diagnosis [18, 19], and have shown great potential in battery material development [11, 20], production process optimization [12], aging mechanism research [21, 22], charging protocol optimization [13], health management [23, 15], and recycling [24].

Different features for battery prognosis and diagnosis are extracted from different data types, including charge/discharge data, impedance data, and relaxation data. The features extracted from charge/discharge data include various instantaneous features, statistical features, and model parameter features extracted from capacity vs. voltage (Q/V) data [25, 26, 27, 28, 29, 30], incremental capacity (dQ/dV) data [31, 32, 33, 34, 24], and differential voltage (dV/dQ) data [31].

Regarding the features extracted from Q/V data, Severson et al. [25] proposed the feature for early battery life prediction based on the discharge Q/V data of the 10th and 100th cycles, $var(\Delta Q_{100-10}/V(V))$, and applied it to accelerate the optimization of fast-charging protocols [13]. Furthermore, Attia et al. [35]

proposed the $IQR(\Delta Q_{100-10}/V(V))$ feature (the IQR of $\Delta Q_{100-10}/V(V)$ represents the difference between the 75th and 25th percentiles of the capacity values in the $\Delta Q_{100-10}/V(V)$ vector) for early battery life prediction based on the same dataset in [25], which outperforms the $var(\Delta Q_{100-10}/V(V))$ feature. Note that the $IQR(\Delta Q_{100-10}/V(V))$ feature inspired the bold thinking of this paper to a great extent. Paulson et al. [11] extracted a total of 396 features from charge and discharge data and studied the impact of feature selection and chemistry type on early battery life prediction. To reduce the demand for charge/discharge data, Jiang et al. [26] and Guo et al. [27] conducted improved early battery life prediction research based on the open-source dataset published in [25], further reducing the demand for test cycles and labeled data. Jiang et al. [26] also proposed to extract the feature $mean(square(\Delta V_{3-2}(Q)))$ from the charge Q/V data for early-cycle classification of battery lifetime. Weng et al. [12] found that the resistance feature measured at 5% SOC after battery formation indicates lithium consumption during the formation process and can be used for cycle life prediction. In terms of reducing the demand for charge/discharge data for diagnostic features, Roman et al. [23], Wang et al. [30], and Lu et al. [29] used different ML models to achieve accurate estimation of SoH using partial charge data.

Since changes in battery voltage may be related to changes in the electrochemical reactions occurring at the two electrodes, voltage change features that characterize the thermodynamic and kinetic states can be utilized for battery prognosis and diagnosis [36, 37, 38, 39, 40, 41]. The features extracted from dQ/dV data and dV/dQ data are voltage change features [42]. Dubarry et al. [31, 32, 33] extracted interpretable instantaneous features, statistical features, and model parameter features from dQ/dV curves and dV/dQ curves for the prognosis and diagnosis of batteries with three different chemistry types (i.e., LFP, NCA, and NMC811). Tao et al. [24] extracted 30 instantaneous and statistical features from charge/discharge Q/V curves and charge/discharge dQ/dV curves for the classification and recycling of batteries with five different chemistry types (i.e., LCO, NMC, LFP, NCA, and NCM-LCO). To reduce the demand for dQ/dV and dV/dQ data in feature engineering, Li et al. [34] extracted the feature $mean(\Delta dQ/dV_{w3-w0}^{(3.6V-3.9V)}(V))$ for early battery life prediction under different usage conditions

from the local (3.60V-3.90V range) $\Delta dQ/dV$ curve obtained by subtracting the dQ/dV data in the reference performance test (RPT) of week 0 from the dQ/dV data in RPT of week 3.

Electrochemical impedance spectroscopy (EIS) is a non-destructive method that can reveal the electrode kinetic processes at different time scales inside the battery, including charge transfer reactions, interface evolution, and mass diffusion [43]. By correlating the impedance evolution with the battery degradation mechanism, EIS provides important insights into the evolution of internal electrochemical processes during battery aging and has become a powerful diagnostic and prognostic tool [44]. Impedance data features include instantaneous and statistical features extracted from EIS and distribution of relaxation times (DRT) data, as well as model parameter features obtained by equivalent circuit model (ECM) fitting. Zhu et al. [45] identified three resistance parameters for characterizing battery SoH by fitting EIS data using ECM. Jones et al. [46] proposed using future cycling protocols and all raw EIS impedances after full discharge (114 real and imaginary impedances at 57 frequencies between 0.02 Hz and 20 kHz) as features for SoH estimation of batteries under uneven usage. Jiang et al. [47] compared the performance of raw EIS impedance features, ECM parameter features, and impedance features at specific frequencies in battery SoH estimation. The comparative test results show that the impedance features at specific frequencies have comprehensive and excellent performance in battery SOH estimation, including accuracy, estimation coverage, and training time. Zhou et al. [48] proposed to use the center coordinates and radius features of the EIS semicircular curve in the high-medium frequency ranges to estimate the battery SoH, and compared them with the ECM parameter features and impedance features at specific frequencies. Test results show the highest SoH estimation accuracy of the center coordinate and radius features. To reduce the demand for EIS data in feature engineering, Zhang et al. [49] determined the importance weights of EIS impedance features at different frequencies through the automatic relevance determination (ARD) of the Gaussian process regression (GPR) model. They found that the two imaginary impedance features in the low-frequency region (17.80 Hz and 2.16 Hz) are sufficient to estimate the battery SoH accurately. Note that this study also inspired the bold thinking of this paper to a great extent.

DRT can directly distinguish the time constants of the main electrochemical processes inside the battery, thereby simplifying EIS analysis [20, 50]. Since the time scale information of the dynamic process inside the battery is closely related to the battery SoH, DRT is becoming a promising technology for battery prognosis and diagnosis [51, 52, 53, 54, 55, 56]. Zhu et al. [57] extracted 12 statistical features from the complete DRT curve and selected five strongly correlated features for battery SoH estimation through the Pearson correlation coefficient. Su et al. [58] extracted 17 features from the DRT curve, including ECM parameter features and statistical features, for battery SoH estimation. Then, eight strongly correlated features are selected through the Spearman correlation coefficient and converted into one indirect feature using the weighted principal component analysis.

In addition to the charge/discharge process, the battery relaxation process after the current is interrupted also contains important battery aging information [59]. After the battery is disconnected from the charge or discharge current, lithium ions continue to diffuse into the active materials, causing the battery voltage to gradually equilibrate with its open circuit voltage (OCV) [60]. The change in relaxation voltage over relaxation time is closely related to loss of Li inventory (*LLI*) and loss of active material *LAM* in battery aging [59, 61, 62], is not limited by charge/discharge protocols [45, 63], and can be used for prognosis and diagnosis [64, 65, 66]. Chen et al. [61, 62] extracted instantaneous and statistical features from the cycle-by-cycle cutoff relaxation voltage data after full charge and discharge to classify the dominant battery aging modes, including solid electrolyte interphase (SEI)-driven *LLI*, Li plating related *LLI*, and *LAM* in positive electrode (*LAM_{PE}*). Zhu et al. [45, 63] used three statistical features (i.e., variance, skewness, and maximum) extracted from the complete voltage relaxation data after full charge to estimate the SoH of batteries from three different manufacturers. To reduce the demand for DRT data in feature engineering, Fan et al. [59] used 10 seconds of relaxation voltage data during a 2-hour relaxation process to estimate the battery SoH.

Batteries are one of the hottest research topics in prognosis and diagnosis [9, 10], and many data-driven battery prognosis and diagnosis methods are published annually. To the best of the authors' knowl-

edge, no data-driven method has answered this fundamental question: What is the minimum amount of data required to extract an accurate feature for battery prognosis and diagnosis? Solving this problem is very important for promoting the field deployment and online application of data-driven methods, especially for large battery systems consisting of hundreds or thousands of cells. Significantly reducing the data requirements for feature engineering means significantly reducing data collection, storage, and computational costs (including time and economic costs) of data-driven methods [67]. Taking the data-driven methods based on EIS data as an example, since the complete EIS measurement process includes impedance measurements at dozens of frequencies in a wide frequency range, the measurement process often takes tens of seconds to several minutes. If the input features need to be extracted from the complete EIS data, it will greatly hinder the field deployment and online application of data-driven methods. Suppose the input features can be extracted from the impedance data corresponding to two high frequencies. In that case, it will facilitate the field deployment and online application of data-driven methods, because some electric vehicles have integrated online impedance measurement functions on DC/DC, and can quickly measure the impedance values corresponding to the two high frequencies. Although hundreds of different battery prognosis and diagnosis features have been proposed for data-driven methods, most rely on a large amount of test data at a specific stage under specific conditions [19]. Although existing studies have made some progress in freeing data-driven methods from their dependence on specific test conditions and data at specific stages [28, 15, 68], the current progress in reducing the data requirements of data-driven methods is far from enough. This paper will conduct a first-principle study to answer the above fundamental question.

Based on the first principle, we start with the simplest single data point and feature selection method (Pearson correlation coefficient), gradually increasing the number of data points. When the number of data points increased to only two, we were pleasantly surprised to find that the best two-point feature (BTPF) obtained by simple subtraction of two data points achieved excellent performance in battery prognosis and diagnosis tasks after simple selection by the Pearson correlation coefficient. Furthermore,

we proposed a general method to extract BTPFs for prognosis and diagnosis tasks from different types of data (including charge/discharge data, impedance data, and relaxation data), and conducted fair comparison tests with multiple state-of-the-art (SOAT) features on six open-source datasets (including 820 Li-ion cells from seven different manufacturers and five different chemistry types). The comparison results show that the accuracy of BTPFs in battery prognosis and diagnosis tasks is comparable to that of SOAT features.

This work challenges the cognition of existing studies on the difficulty of battery prognosis and diagnosis tasks. Existing studies generally believe that accurate battery prognosis and diagnosis is challenging [25, 10] due to the complex coupling of many factors in battery design (significant variability in materials, chemistry types, and structures), production (significant variability in manufacturers, production equipment, and processes), and usage (significant variability in device, fields, and operating conditions) [69]. This paper proposes a general BTPF extraction method for battery prognosis and diagnosis tasks based on only two data points and the simplest Pearson correlation coefficient. We test the performance of BTPFs against existing SOAT features using different types of data from hundreds of battery cells. The results of this paper will prompt researchers to rethink and re-evaluate the difficulty of battery prognosis and diagnosis tasks.

This work overturns the fixed pattern of establishing data-driven prognosis and diagnosis methods for complex dynamical systems through deliberate feature engineering. Based on the first principle, this paper attempts to use the simplest single data point and feature selection method (Pearson correlation coefficient), gradually increasing the number of data points. It is ultimately determined that two data points are the minimum amount of data required to extract an accurate prognostic and diagnostic feature, answering the above fundamental question. The BTPF extraction method proposed in this paper provides a new direction for feature engineering of complex dynamical systems. Moreover, the BTPF extraction method provides a new benchmark for feature engineering of data-driven battery prognosis and diagnosis methods.

This work highlights the promise of data-driven field battery prognostic and diagnostic methods. Taking EIS data as an example, the BTPF dramatically reduces the dozens of frequencies required for a complete EIS measurement to two frequencies, significantly shortening the measurement time and making it possible to perform battery prognosis and diagnosis through online impedance measurement at two specific frequencies. It is worth mentioning that some electric vehicles have already integrated the online impedance measurement function on DCDC [70, 71]. In addition, for large battery systems consisting of hundreds or thousands of cells, such as those in passenger cars [72] and energy storage stations [73], the use of two-point features can significantly reduce the data collection, storage, and computational costs required for prognosis and diagnosis of each cell, helping to promote the deployment of simpler and faster battery prognostic and diagnostic methods in different fields.

2. Data

In this paper, six open-source battery datasets are selected to test the proposed BTPF extraction method. These datasets contain 820 Li-ion cells with seven different manufacturers, five chemistry types, and three data types, as shown in **Supplementary Table 1**. For ease of reference, we number these open-source datasets as Dataset 1 to Dataset 6. Among them, Dataset 1 and Dataset 2 are used for the prognosis task. Dataset 1 has variable charging protocols and a constant discharging protocol, and Dataset 7 has variable charging and discharging protocols. The features used for the prognosis task in Dataset 1 are extracted from the discharge Q/V data in different cycles, and the features used for the prognosis task in Dataset 7 are extracted from the discharge dQ/dV and dV/dQ data in different periodic RPTs. Dataset 3 and Dataset 4 are used for the diagnosis task. Dataset 3 has variable charging and discharging protocols, and Dataset 4 has constant charging and discharging protocols. The features used for the diagnosis task in Dataset 3 are extracted from the EIS data after full discharge in each cycle, and the features used for the diagnosis task in Dataset 4 are extracted from the EIS data after full charge in each cycle. Dataset 5 and Dataset 6 are used for the diagnosis task, both of which have variable charging and discharging

protocols. The features used for the diagnosis task in Dataset 5 are extracted from the relaxation V/t data after full charge in each cycle, and the features used for the diagnosis task in Dataset 6 are extracted from the relaxation V/t data after full discharge in each periodic RPT.

To compare the BTPF with SOAT features in recent publications, this paper also uses capacity to characterize the battery SoH. Meanwhile, the cycle number corresponding to the full discharge capacity decay to 80% of the nominal capacity is used as the battery cycle life. For more detailed dataset and cell descriptions, please refer to the corresponding references in **Supplementary Table 1**, which will not be repeated here.

3. Methods

As shown in Figure 1, the BTPF extraction method are proposed for battery prognosis and diagnosis tasks, which mainly includes four steps: (1) Data collection. (2) Difference calculation. (3) Feature extraction. (4) Feature selection.

The detailed steps of the BTPF extraction method for the prognosis task are: (1) Data collection. Collect the target data in two specific battery cycles (such as the 10th and 100th cycles in [25]). The data types include charge/discharge Q/V data, charge/discharge dQ/dV data, charge/discharge dV/dQ data, EIS data, DRT data, and relaxation V/t data after charge/discharge. (2) Difference calculation. Firstly, the target data collected in two specific cycles is standardized to facilitate subsequent calculations. The spline function is utilized to fit the target data and a unified linear interpolation is performed. For the charge/discharge Q/V data, the capacity is fitted as a function of voltage and evaluated with same linearly spaced voltage points. For the charge/discharge dQ/dV data, the incremental capacity is fitted as a function of voltage and evaluated with same linearly spaced voltage points. For the charge/discharge dV/dQ data, the differential voltage is fitted as a function of capacity and evaluated with same linearly spaced capacity points. For the relaxation V/t data after charge/discharge, the relaxation voltage is fitted as a function of relaxation time and evaluated with same linearly spaced time points. Then, subtract the

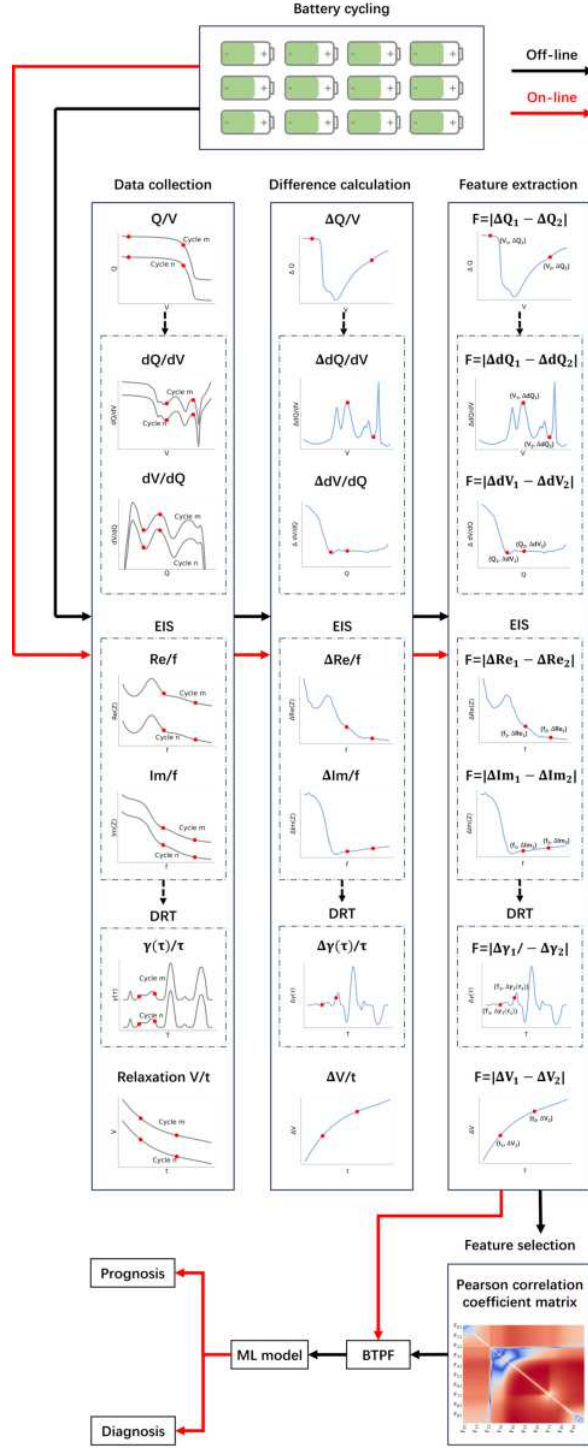


Figure 1: The BTPF extraction method for battery prognosis and diagnosis tasks.

fitted target data in the lower cycle from that of the higher cycle to obtain the difference curve, which can be one of the charge/discharge capacity difference ($\Delta Q/V$) curve, charge/discharge incremental capacity difference ($\Delta dQ/dV$) curve, charge/discharge differential voltage difference ($\Delta dV/dQ$) curve, and relaxation voltage difference ($\Delta V/t$) curve after charge/discharge. It should be mentioned that since the frequency and time data points of EIS and DRT curves in different cycles are originally the same, there is no need to perform spline function fitting and unified linear interpolation. We can directly subtract the original EIS and DRT data in the lower cycle from that in the higher cycle to obtain the real impedance difference ($\Delta Re/f$) curve, the imaginary impedance difference ($\Delta Im/f$) curve, and the DRT difference ($\Delta \gamma(\tau)/\tau$) curve. (3) Feature extraction. Extract candidate two-point features from the difference curve. Subtract the ordinate values corresponding to any two abscissa values on the differential curve and take the absolute value as a candidate two-point feature. Traverse all combinations of two abscissa values on the differential curve, and a total of $(n^2 - n)/2$ candidate two-point features can be obtained, where n is the number of abscissa values on the differential curve. Further, all candidate two-point features are obtained by traversing all cells in the training set. (4) Feature selection. The Pearson correlation coefficient between each candidate two-point feature and the cycle life of all cells in the training set is calculated, and the feature corresponding to the Pearson correlation coefficient with the largest absolute value is selected as the BTPF. The BTPFs of all cells in the training set are used as input and the corresponding cycle life of all cells in the training set is used as output to train the ML regression model. When making an online prognosis, only two target data points in two specific cycles need to be collected to calculate the BTPF. Then, the BTPF is input into the trained ML regression model to predict the cycle life of the target cell.

The detailed steps of the two-point feature extraction method for the diagnosis task are: (1) Data collection. Collect targeted data in every cycle throughout the cell life. The data types include charge/discharge Q/V data, charge/discharge dQ/dV data, charge/discharge dV/dQ data, EIS data, DRT data, and relaxation V/t data after charge/discharge. (2) Difference calculation. Firstly, the target data collected in each cycle is standardized to facilitate subsequent calculations. The spline function is utilized to fit the

target data and a unified linear interpolation is performed. For the charge/discharge Q/V data, the capacity is fitted as a function of voltage and evaluated with same linearly spaced voltage points. For the charge/discharge dQ/dV data, the incremental capacity is fitted as a function of voltage and evaluated with same linearly spaced voltage points. For the charge/discharge dV/dQ data, the differential voltage is fitted as a function of capacity and evaluated with same linearly spaced capacity points. For the relaxation V/t data after charge/discharge, the relaxation voltage is fitted as a function of relaxation time and evaluated with same linearly spaced time points. Then, subtract the fitted target data in the first cycle from that of the higher cycle to obtain the difference curve, which can be one of the charge/discharge $\Delta Q/V$ curves, charge/discharge $\Delta dQ/dV$ curves, charge/discharge $\Delta dV/dQ$ curves, and relaxation $\Delta V/t$ curves after charge/discharge. It should be mentioned that since the frequency and time data points of EIS and DRT curves in different cycles are originally the same, there is no need to perform spline function fitting and unified linear interpolation. We can directly subtract the original EIS and DRT data in the first cycle from that in higher cycles to obtain the $\Delta Re/f$ curves, the $\Delta Im/f$ curves, and the $\Delta \gamma(\tau)/\tau$ curves. (3) Feature extraction. Extract candidate two-point features from the difference curve. Subtract the ordinate values corresponding to any two abscissa values on the differential curve and take the absolute value as a candidate two-point feature. Traverse all combinations of two abscissa values on the differential curve, and a total of $(n^2 - n)/2$ candidate two-point features can be obtained, where n is the number of abscissa values on the differential curve. Further, all candidate two-point features are obtained by traversing all cells in the training set. (4) Feature selection. The Pearson correlation coefficient between each candidate two-point feature and the cycle capacities of all cells in the training set is calculated, and the feature corresponding to the Pearson correlation coefficient with the largest absolute value is selected as the BTPF. The BTPFs of all cells in the training set are used as input and the corresponding cycle capacities of all cells in the training set is used as output to train the ML regression model. When making an online diagnosis, only two target data points in the first cycle and the target cycle need to be collected to calculate the BTPF. Then, the BTPF is input into the trained ML regression model to estimate the SoH of the target

cell.

4. Results

The comparison results of the BTPF proposed in this paper and the recent SOAT features on different datasets are shown in Tables 1 to 6. The detailed results for each dataset are presented below.

Table 1: Comparison results of the BTPF and SOAT features on 124 cells in Dataset 1. The BTPF (Q/V) represents the feature $PTP_{DIS:2.735V-2.900V} \triangle Q_{100-10}/V(V)$ and the SOAT feature represents the feature $var(\triangle Q_{100-10}/V(V))$ proposed in [25].

Dataset 1						
	Training set		Primary test set		Secondary test set	
Metrics	BTPF (Q/V)	SOAT [25]	BTPF (Q/V)	SOAT [25]	BTPF (Q/V)	SOAT [25]
MAE (cycles)	42.6	44.9	91.1	73.9	148.4	138.4
MAPE (%)	5.3	5.8	12.4	9.3	13.9	12.6
RMSE (cycles)	73	75	129	117	197	191
$R^2(-)$	0.94	0.95	0.89	0.91	0.58	0.61
Data used in one cycle (in two cycles)	2 (4)	About 800 (1600)	2 (4)	About 800 (1600)	2 (4)	About 800 (1600)

4.1. Performance on the prognosis task

4.1.1. Dataset 1

For Dataset 1, the BTPF extraction method for battery prognosis task is shown in **Supplementary Figure 1**. To make a fair comparison with the SOAT feature $var(\triangle Q_{100-10}/V(V))$ proposed by Severson et al. [25], this paper uses the same training and test sets as [25]. Specifically, Dataset 1 contains 169 LFP cells with nominal capacity of 1.1 Ah. Among them, the first 124 cells are published by Severson et al. [25], the remaining 45 cells are published by Attia et al. [13]. The 124 LFP cells are divided into three sub-datasets, namely the training set (41 cells), the primary test set (43 cells), and the secondary test set (40 cells). All remaining 45 cells are used as the third test set. The training set is utilized to train the ML regression model, and the test sets are utilized to verify and test the predictive performance of the trained

Table 2: Comparison results of the BTPF and SOAT features on 225 cells in Dataset 2. The BTPF (dQ/dV) represents the feature $PTP_{DIS:3.648V-4.080V} \triangle dQ_{w3-w0}/dV(V)$, the BTPF (dV/dQ) represents the feature $PTP_{DIS:0.2016Ah-0.2324Ah} \triangle dV_{w3-w0}/dQ(Q)$, and the SOAT feature represents the feature $mean(\triangle dQ/dV_{w3-w0}^{3.6V-3.9V}(V))$ proposed in [34].

Dataset 2						
High-DoD training set			High-DoD test set			
Metrics	BTPF (dQ/dV)	BTPF (dV/dQ)	SOAT [34]	BTPF (dQ/dV)	BTPF (dV/dQ)	SOAT [34]
MAE (cycles)	3.09	0.96	2.66	2.92	1.05	2.52
MAPE (%)	24.8	23.5	17.1	20.0	16.4	18.3
RMSE (cycles)	1.50	1.27	1.55	1.67	1.44	1.84
$R^2(-)$	0.68	0.76	0.66	0.58	0.69	0.49
Data used in one cycle (in two cycles)	2 (4)	2 (4)	250 (500)	2 (4)	2 (4)	250 (500)

Low-DoD test set						
Metrics	BTPF (dQ/dV)	BTPF (dV/dQ)	SOAT [34]			
MAE (cycles)	8.19	6.76	7.71			
MAPE (%)	30.6	33.2	28.6			
RMSE (cycles)	5.11	8.03	5.27			
$R^2(-)$	0.18	0.25	0.03			
Data used in one cycle (in two cycles)	2 (4)	2 (4)	250 (500)			

ML regression model. For more details about the training and test sets, please refer to [25, 13] and will not be repeated here.

Data collection: Similar to [25], the discharge Q/V data in the 10th and 100th cycles are collected (the constant current-constant voltage (CC-CV) discharge mode is used, the discharge current in the CC stage is 4C, the discharge cut-off voltage in the CC stage is 2.0V, and the cut-off discharge current in the CV stage is C/50) for feature extraction.

Difference calculation: The discharge Q/V data collected in the 10th and 100th cycles are standardized to facilitate subsequent calculations. Specifically, the spline function is utilized to fit the discharge Q/V data in the CC stage, and a unified linear interpolation is performed. The discharge capacity is fitted as a function of the discharge voltage, and the discharge voltage is linearly divided into 100 values between 3.5 V and 2.0 V at intervals of 15 mV, as shown in **Supplementary Figure 2(a)**. It should be

Table 3: Comparison results of the BTPF and SOAT features on 40 cells in Dataset 3. The BTPF (EIS) represents the feature $DTP_{ADIS:1922.08Hz-4.36Hz} \triangle Re_{n-1}/f(f)$, the BTPF (DRT) represents the feature $DTP_{ADIS:1.23e-4-5.41e-3} \triangle \gamma(\tau)_{n-1}/\tau$, and the SOAT feature represents the raw EIS impedances proposed in [46].

Dataset 3						
Training set				Test set		
Metrics	BTPF (EIS)	BTPF (DRT)	SOAT [46]	BTPF (EIS)	BTPF (DRT)	SOAT [46]
MAE (mAh)	2.74	2.96	2.60	2.90	2.86	3.41
MAPE (%)	10.60	11.50	10.40	11.61	11.51	13.41
RMSE (mAh)	3.33	3.64	3.14	3.55	3.59	4.27
$R^2(-)$	0.69	0.63	0.72	0.65	0.65	0.49
Data used in one cycle (in two cycles)	2 (4)	2 (4)	57 (-)	2 (4)	2 (4)	57 (-)

Table 4: Comparison results of the BTPF and SOAT features on 8 cells in Dataset 4. The BTPF (EIS) represents the feature $DTP_{ACH:115.778Hz-11.145Hz} \triangle Im_{n-1}/f(f)$, the BTPF (DRT) represents the feature $DTP_{ACH:0.003s-14.42s} \triangle \gamma(\tau)_{n-1}/\tau$, and the SOAT feature represents the raw EIS impedances proposed in [49].

Dataset 4						
Training set				Test set		
Metrics	BTPF (EIS)	BTPF (DRT)	SOAT [49]	BTPF (EIS)	BTPF (DRT)	SOAT [49]
MAE (mAh)	0.58	0.73	0.87	2.95	2.33	2.45
MAPE (%)	2.08	2.59	3.08	12.82	10.06	11.32
RMSE (mAh)	0.86	0.92	0.81	3.77	3.38	3.57
$R^2(-)$	0.90	0.89	0.89	0.29	0.53	0.35
Data used in one cycle (in two cycles)	2 (4)	2 (4)	60 (-)	2 (4)	2 (4)	60 (-)

noted here that in [25], the discharge voltage is linearly divided into 1000 values between 3.5 V and 2.0 V at intervals of 1.5 mV. To reduce the computational burden, this paper uses a larger voltage division interval of 15mV than 1.5mV in [25]. Increasing the voltage interval does not affect the fairness of the comparison. The fitted discharge Q/V data in the two cycles are subtracted (the discharge Q/V data in the 100th cycle minus the discharge Q/V data in the 10th cycle) to obtain the discharge $\triangle Q_{100-10}/V$ curve. As shown in **Supplementary Figure 2(b)**, the obtained discharge $\triangle Q_{100-10}/V$ curve is the shaded part between the two discharge Q/V curves in the 10th and 100th cycles. The discharge $\triangle Q_{100-10}/V$ curves

Table 5: Comparison results of the BTPF and SOAT features on cells in Dataset 5. The BTPF (V/t) represents the feature $DTP_{ACH:0s-936s} \triangle V_{n-1}/t(t)$ and the SOAT feature represents the features [Var, Ske, Max] proposed in [45].

Dataset 5				
Metrics	Training set		Test set	
	BTPF (V/t)	SOAT [45]	BTPF (V/t)	SOAT [45]
MAE (mAh)	0.003	0.002	0.013	0.011
MAPE (%)	0.358	0.241	1.644	1.328
RMSE (mAh)	0.004	0.003	0.018	0.016
$R^2(-)$	0.958	0.982	0.921	0.943
Data used in one cycle (in two cycles)	2 (4)	15 (-)	2 (4)	15 (-)

Table 6: Comparison results of the BTPF and SOAT features on cells in Dataset 6. The BTPF (V/t) represents the feature $DTP_{ADIS:6120s-6984s} \triangle V_{n-1}/t(t)$ and the SOAT feature represents the features [Var, Ske, Max] proposed in [45].

Dataset 6				
Metrics	Training set		Test set	
	BTPF (V/t)	SOAT [45]	BTPF (V/t)	SOAT [45]
MAE (mAh)	0.14	0.15	0.16	0.16
MAPE (%)	0.19	0.28	0.14	0.16
RMSE (mAh)	0.22	0.23	0.22	0.23
$R^2(-)$	0.86	0.85	0.87	0.85
Data used in one cycle (in two cycles)	2 (4)	720 (-)	2 (4)	720 (-)

of first 124 cells in Dataset 1 [25] are shown in **Supplementary Figure 2(c)**.

Feature extraction: The capacity difference ($\triangle Q_{100-10}$) values corresponding to any two voltage values on the discharge $\triangle Q_{100-10}/V$ curve are subtracted and the absolute value is taken as a candidate two-point feature, as shown in **Supplementary Figure 3**. Since the discharge voltage is linearly divided into 100 values between 3.5 V and 2.0 V in this paper, a total of $(100^2 - 100)/2 = 4950$ candidate two-point features can be obtained by traversing all combinations of two voltage values on the discharge $\triangle Q_{100-10}/V$ curve, as shown in Figure 2(a).

Feature selection: The Pearson correlation coefficient between each candidate two-point feature

and the cycle life of 41 cells in the training set is calculated, and the candidate two-point feature corresponding to the correlation coefficient with the largest absolute value of 0.873 is selected as the BTPF $PTP_{DIS:2.735V-2.900V} \triangle Q_{100-10}/V(V)$, as shown in Figure 2(a). For $PTP_{DIS:2.735V-2.900V} \triangle Q_{100-10}/V(V)$, PTP represents a two-point feature for the prognosis task, $DIS: 2.735V - 2.900V$ represents that the two-point feature extraction uses the two discharge $\triangle Q$ values corresponding to the two discharge voltages 2.735V and 2.900V, $\triangle Q_{100-10}/V$ represents that the two-point feature extraction uses the $\triangle Q_{100-10}/V$ curve obtained by subtracting the Q/V data in the 10th cycle from the Q/V data in the 100th cycle, and (V) represents that the Q/V data is fitted as a function of voltage. The two data points on the $\triangle Q_{100-10}/V$ curve that utilized to calculate $PTP_{DIS:2.735V-2.900V} \triangle Q_{100-10}/V(V)$ are shown in **Supplementary Figure 2(c)**. The distribution relationship between the cycle life of all 124 cells in Dataset 1 and $PTP_{DIS:2.735V-2.900V} \triangle Q_{100-10}/V(V)$ is shown in Figure 2(b). The Pearson correlation coefficient is 0.851, which is lower than that of feature $var(\triangle Q_{100-10}/V(V))$ (0.93 in [25]), as shown in **Supplementary Figure 4**.

Cycle life prediction: Combining the BTPF $PTP_{DIS:2.735V-2.900V} \triangle Q_{100-10}/V(V)$ and the XGBoost regression model, the cell cycle life prediction results of first 124 cells in Dataset 1 are shown in Figure 3(a). For more detailed XGBoost regression model training and hyperparameter adjustment, please refer to **Supplementary Note 1**. Combining the feature $var(\triangle Q_{100-10}/V(V))$ [25] and the XGBoost regression model of this paper (using exactly the same model training and hyperparameter adjustment method), the cell cycle life prediction results of first 124 cells in Dataset 1 are shown in Figure 3(b). The cell cycle life prediction results of different features on the training set, primary test set, and secondary test set are shown in Table 1. More detailed results are shown in **Supplementary Tables 2 to 4**. In this paper, the matrices of mean absolute error (MAE), mean absolute percentage error (MAPE), root mean square error (RMSE), and R^2 are chosen to evaluate XGBoost regression model performance in the prognosis and diagnosis tasks. For more detailed matrices introduction, please refer to **Supplementary Note 2**. It can be found that $PTP_{DIS:2.735V-2.900V} \triangle Q_{100-10}/V(V)$ achieves a comparable accuracy to that of

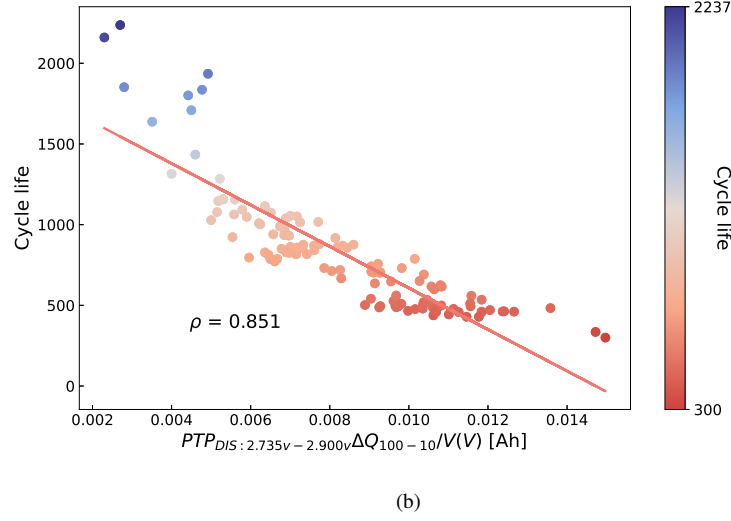
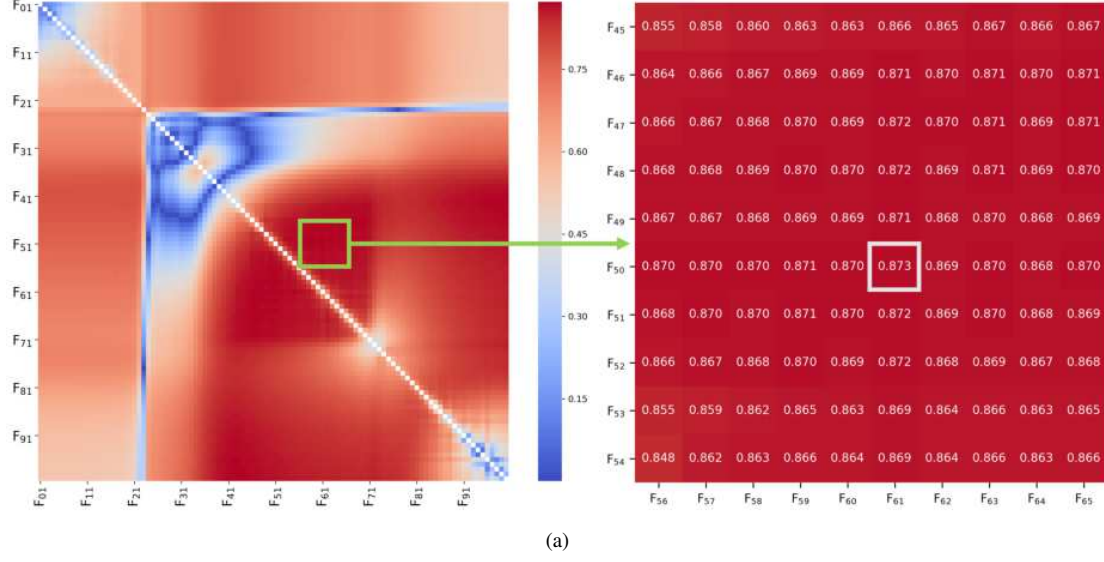


Figure 2: (a) Selection of the BTPF using the Pearson correlation coefficient between each candidate two-point feature and the cycle life of 41 cells in the training set. F01 to F100 represent 100 values of discharge voltage from 2.0 V to 3.5 V, with an interval of 15 mV. The colors are determined based on the Pearson correlation coefficient values. (b) Cycle life of first 124 cells in Dataset 1 plotted as a function of $PTP_{DIS:2.735V-2.900V} \Delta Q_{100-10}/V(V)$, with a Pearson correlation coefficient of 0.851. The colors are determined based on the cycle life of cells.

$var(\Delta Q_{100-10}/V(V))$ [25], while $var(\Delta Q_{100-10}/V(V))$ [25] uses about 800 discharge Q/V data points in each cycle, which is about 400 times that of $PTP_{DIS:2.735V-2.900V} \Delta Q_{100-10}/V(V)$. Fewer data points mean less data collection, storage, and computational costs.

Furthermore, the third test set with 45 cells [13] in Dataset 1 is utilized to test the generalizability of $PTP_{DIS:2.735V-2.900V} \Delta Q_{100-10}/V(V)$, and the previously trained XGBoost regression model is directly used for prediction. The test results are shown in **Supplementary Figure 5** and **Supplementary Table 4**.

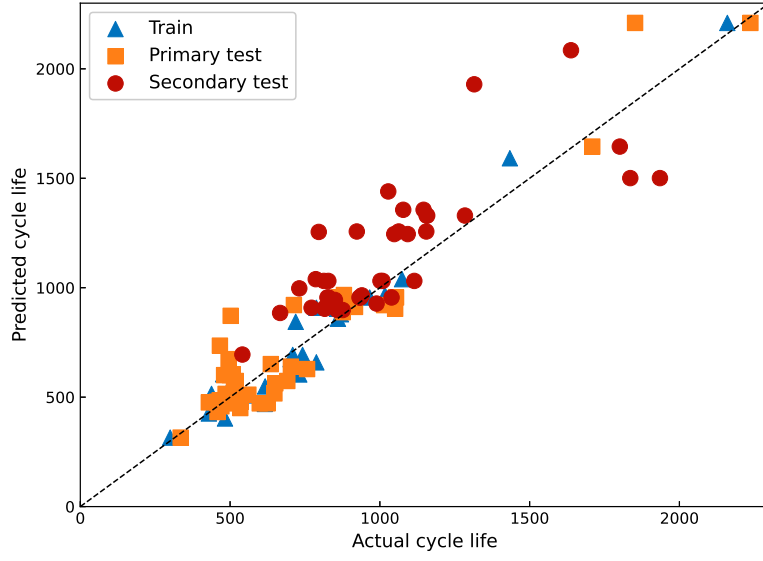
4.1.2. Dataset 2

(1) BTPF extraction from dQ/dV data

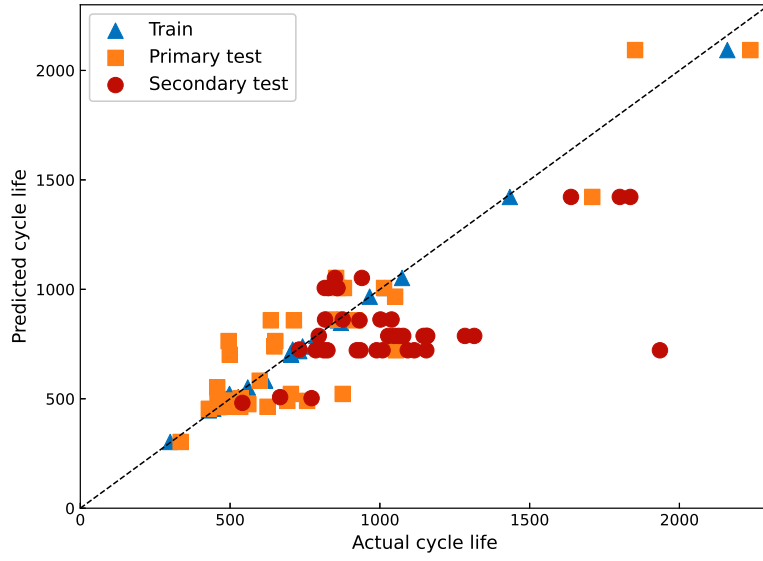
For Dataset 2, the BTPF extraction method for battery prognosis task is shown in **Supplementary Figure 6**. To make a fair comparison with the SOAT feature $mean(\Delta dQ/dV_{w3-w0}^{3.6V-3.9V}(V))$ proposed by Li et al. [34], this paper uses the same training and test sets as [34]. Specifically, Dataset 2 containing 225 NMC cells is divided into three sub-datasets according to the depth of discharge (DOD), namely the high-DoD training set (116 cells), the high-DoD test set (60 cells), and the low-DoD test set (49 cells). The high-DoD training set is utilized to train the ML regression model, and the high-DoD test set and the low-DoD test set are utilized to verify and test the prediction performance of the trained ML regression model. For more details about the training and test sets, please refer to [34] and will not be repeated here.

Data collection: Similar to [34], the discharge Q/V data in the periodic RPTs of week 0 and week 3 are collected (CC discharge mode is used, the discharge current is C/5, and discharge cut-off voltage is 3.0V) and dQ/dV curves are calculated for feature extraction.

Difference calculation: Discharge dQ/dV curves in two periodic RPTs are standardized to facilitate subsequent calculation calculations, as shown in **Supplementary Figure 7(a)**. The fitted discharge dQ/dV curves in the two RPTs are subtracted to obtain the discharge $\Delta dQ_{w3-w0}/dV$ curve, as shown in **Supplementary Figure 7(b)**. The discharge $\Delta dQ_{w3-w0}/dV$ curves of all 225 cells in Dataset 2 are



(a)



(b)

Figure 3: Cycle life prediction results of of first 124 cells in Dataset 1. (a) Cycle life prediction results of $PTP_{DIS:2.735V-2.900V} \triangle Q_{100-10}/V(V)$. The input of XGBoost regression model is $PTP_{DIS:2.735V-2.900V} \triangle Q_{100-10}/V(V)$, and the output is the cell cycle life. (b) Cycle life prediction results of $var(\triangle Q_{100-10}/V(V))$ [25]. The input of the XGBoost regression model is $var(\triangle Q_{100-10}/V(V))$, and the output is the cell cycle life.

shown in **Supplementary Figure 7(c)**.

Feature extraction: The incremental capacity difference (ΔdQ_{w3-w0}) values corresponding to any two voltage values on the discharge $\Delta dQ_{w3-w0}/dV$ curve are subtracted and the absolute value is taken as a candidate two-point feature, as shown in **Supplementary Figure 8**. A total of $(100^2 - 100)/2 = 4950$ candidate two-point features can be obtained by traversing all combinations of two voltage values on the discharge $\Delta dQ_{w3-w0}/dV$ curve.

Feature selection: The Pearson correlation coefficient between each candidate two-point feature and the week life of all 116 cells in the training set is calculated, and the candidate two-point feature corresponding to the correlation coefficient with the largest absolute value of 0.892 is selected as the BTPF $PTP_{DIS:3.648V-4.080V} \Delta dQ_{w3-w0}/dV(V)$, as shown in Figure 4(a). The two data points on the $\Delta dQ_{w3-w0}/dV$ curve that utilized to calculate $PTP_{DIS:3.648V-4.080V} \Delta dQ_{w3-w0}/dV(V)$ are shown in **Supplementary Figure 7(c)**. The distribution relationship between the week life of all 225 cells in Dataset 2 and $PTP_{DIS:3.648V-4.080V} \Delta dQ_{w3-w0}/dV(V)$ is shown in Figure 4(b). The Pearson correlation coefficient is 0.827, which is slightly lower than that of $\log(\text{mean}(\Delta dQ/dV_{w3-w0}^{3.6V-3.9V}(V)))$ (0.848 in [34]), as shown in **Supplementary Figure 9**.

Week life prediction: Combining the BTPF $PTP_{DIS:3.648V-4.080V} \Delta dQ_{w3-w0}/dV(V)$ and the XGBoost regression model, the cell week life prediction results are shown in Figure 5(a). Combining the feature $\text{mean}(\Delta dQ/dV_{w3-w0}^{3.6V-3.9V}(V))$ [34] and the XGBoost regression model, the cell week life prediction results are shown in Figure 5(b).

The cell week life prediction results of different features on the high-DoD training set, high-DoD test set, and low-DoD test set are shown in Table 2. More detailed results are shown in **Supplementary Tables 6 to 8**. It can be found that $PTP_{DIS:3.648V-4.080V} \Delta dQ_{w3-w0}/dV(V)$ achieves a comparable accuracy to that of $\log(\text{mean}(\Delta dQ/dV_{w3-w0}^{3.6V-3.9V}(V)))$ [34], while $\log(\text{mean}(\Delta dQ/dV_{w3-w0}^{3.6V-3.9V}(V)))$ uses about 250 discharge Q/V data points, which is about 125 times that of $PTP_{DIS:3.648V-4.080V} \Delta dQ_{w3-w0}/dV(V)$. Fewer data points mean less data collection, storage, and computational costs.

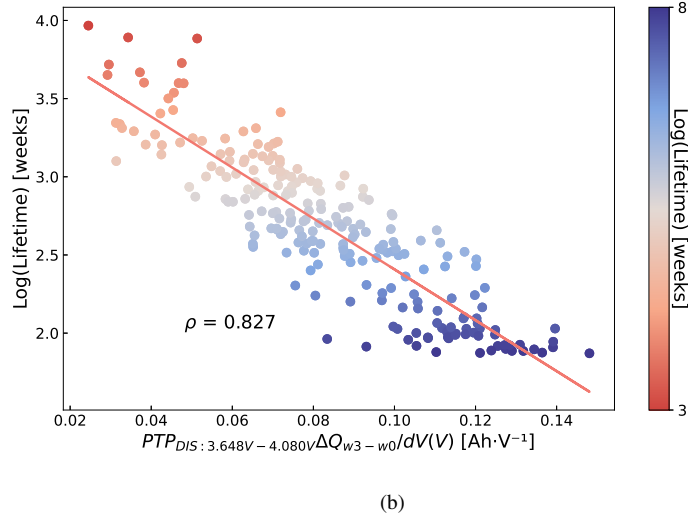
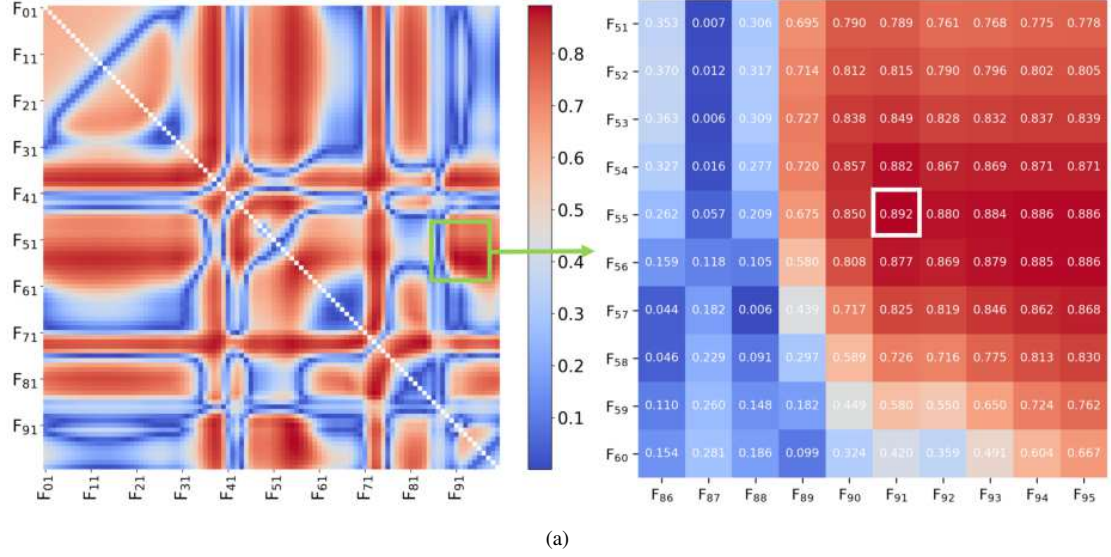
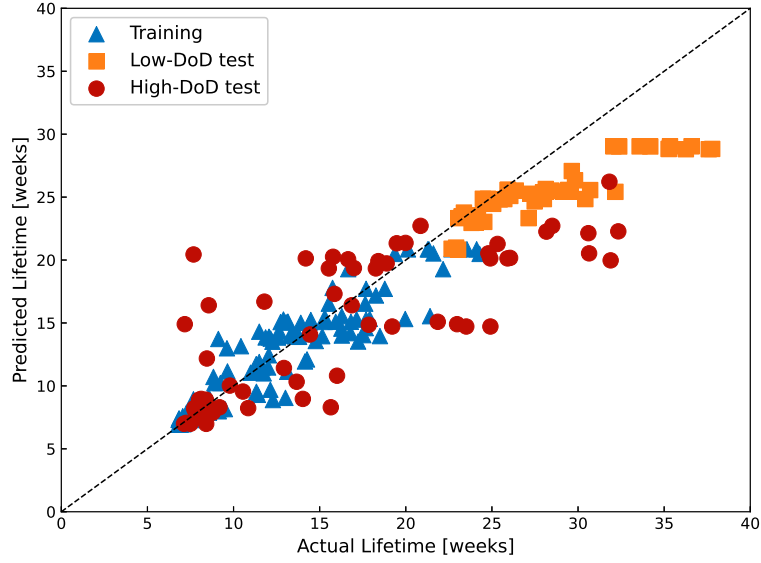
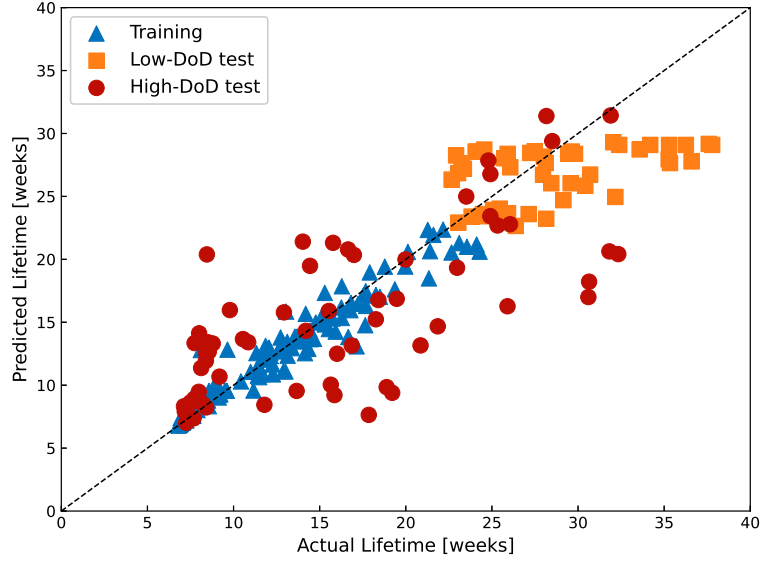


Figure 4: (a) Selection of the BTPF using the Pearson correlation coefficient between each candidate two-point feature and the week life of 116 cells in the training set. F01 to F100 represent 100 values of discharge voltage from 3.0 V to 4.2 V at intervals of 12 mV. The colors are determined based on the Pearson correlation coefficient values. (b) Week life of 225 cells in Dataset 2 plotted as a function of $PTP_{DIS:3.648V-4.080V} \Delta Q_{w3-w0}/dV(V)$, with a Pearson correlation coefficient of 0.827. The colors are determined based on the week life of cells.



(a)



(b)

Figure 5: Week life prediction results of 225 cells in Dataset 2. (a) The week life prediction results of $PTP_{DIS:3.648V-4.080V} \triangle dQ_{w3-w0}/dV(V)$. The input of XGBoost regression model is $PTP_{DIS:3.648V-4.080V} \triangle dQ_{w3-w0}/dV(V)$, and the output is the cell week life. (b) The week life prediction results of $\log(\text{mean}(\triangle dQ/dV_{w3-w0}^{3.6V-3.9V}(V)))$ [34]. The input of the XGBoost regression model is $\log(\text{mean}(\triangle dQ/dV_{w3-w0}^{3.6V-3.9V}(V)))$, and the output is the cell week life.

Furthermore, $PTP_{DIS:3.648V-4.080V} \triangle dQ_{w3-w0}/dV(V)$ and $\log(\text{mean}(\triangle dQ/dV_{w3-w0}^{3.6V-3.9V}(V)))$ are combined with the other two features proposed in [34], $\log(|\triangle CVTime_{w0}|)$ and DoD , to predict the week life of cells in Dataset 2. The prediction results are shown in **Supplementary Figure 10**. The prediction results of different features are shown in **Supplementary Tables 9 to 11**.

(2) BTPF extraction from dV/dQ data

Similar to the BTPF extracted from the discharge dQ/dV data (**Supplementary Figure 6(a)**), we also can extract the BTPF from the discharge dV/dQ data, as shown in **Supplementary Figure 6(b)**.

Data collection: Similar to [34], the discharge Q/V data in the periodic RPTs of week 0 and week 3 are collected and dV/dQ curves are calculated for feature extraction.

Difference calculation: Discharge dV/dQ curves in two periodic RPTs are standardized to facilitate subsequent calculation calculations, as shown in **Supplementary Figure 11(a)**. The fitted discharge dV/dQ curves in the two RPTs are subtracted to obtain the discharge $\triangle dV_{w3-w0}/dQ$ curve, as shown in **Supplementary Figure 11(b)**. The discharge $\triangle dV_{w3-w0}/dQ$ curves of all 225 cells in Dataset 2 are shown in **Supplementary Figure 11(c)**.

Feature extraction: The differential voltage difference ($\triangle dV_{w3-w0}$) values corresponding to any two capacity values on the discharge $\triangle dV_{w3-w0}/dQ$ curve are subtracted and the absolute value is taken as a candidate two-point feature, as shown in **Supplementary Figure 12**. A total of $(100^2 - 100)/2 = 4950$ candidate two-point features can be obtained by traversing all combinations of two capacity values on the discharge $\triangle dV_{w3-w0}/dQ$ curve.

Feature selection: The Pearson correlation coefficient between each candidate two-point feature and the week life of 116 cells in the high-DOD training set is calculated, and the candidate two-point feature corresponding to the correlation coefficient with the largest absolute value of 0.886 is selected as the BTPF $PTP_{DIS:0.2016Ah-0.2324Ah} \triangle dV_{w3-w0}/dQ(Q)$, as shown in Figure 6(a). The two data points on the $\triangle dV_{w3-w0}/dQ$ curve utilized to calculate $PTP_{DIS:0.2016Ah-0.2324Ah} \triangle dV_{w3-w0}/dQ(Q)$ are shown in **Supplementary Figure 11(c)**. The distribution relationship between the week life of all 225 cells in Dataset

2 and $PTP_{DIS:0.2016Ah-0.2324Ah} \triangle dV_{w3-w0}/dQ(Q)$ is shown in Figure 6(b). The Pearson correlation coefficient is 0.805.

Week life prediction: Combining the BTPF $PTP_{DIS:0.2016Ah-0.2324Ah} \triangle dV_{w3-w0}/dQ(Q)$ and the XGBoost regression model, the cell week life prediction results are shown in Figure 7 and Table 2. More detailed results are shown in **Supplementary Tables 12 to 14**.

Furthermore, $PTP_{DIS:0.2016Ah-0.2324Ah} \triangle dV_{w3-w0}/dQ(Q)$ is combined with the other two features proposed in [34], $\log(|\triangle CVTime_{w0}|)$ and DoD , to predict the week life of cells in Dataset 2. The prediction results are shown in **Supplementary Figure 13** and **Supplementary Tables 12 to 14**. It can be found that $PTP_{DIS:0.2016Ah-0.2324Ah} \triangle dV_{w3-w0}/dQ(Q)$ achieves a comparable accuracy to that of $\log(mean(\triangle dQ/dV_{w3-w0}^{3.6V-3.9V}(V)))$ [34], while $\log(mean(\triangle dQ/dV_{w3-w0}^{3.6V-3.9V}(V)))$ uses about 250 discharge Q/V data points, which is about 125 times that of $PTP_{DIS:0.2016Ah-0.2324Ah} \triangle dV_{w3-w0}/dQ(Q)$. Fewer data points mean less data collection, storage, and computational costs.

4.1.3. Rationalization of prognostic performance

The aging of Li-ion batteries mainly include changes in the amount of active materials (called *LAM*), which may occur at both the anode and cathode) and changes in the amount of reacted lithium (called *LLI*). Results in [25] and [74] show that for the incremental capacity curve and differential voltage curve calculated from the charge/discharge Q/V curves, the change in the main peak of the incremental capacity curve can quantitatively characterize *LAM*, and the movement trend of the differential voltage curve can quantitatively characterize *LLI*. Similar to the features $var(\triangle Q_{100-10}(V))$ and $mean(\triangle dQ/dV_{w3-w0}^{(3.6V-3.9V)}(V))$ proposed in [25, 34], the BTPFs proposed in this paper is also extracted from two discharge Q/V curves in different cycles. We attribute the success of BTPFs in the prognosis task to capturing the changing trends of *LAM* and *LLI*.

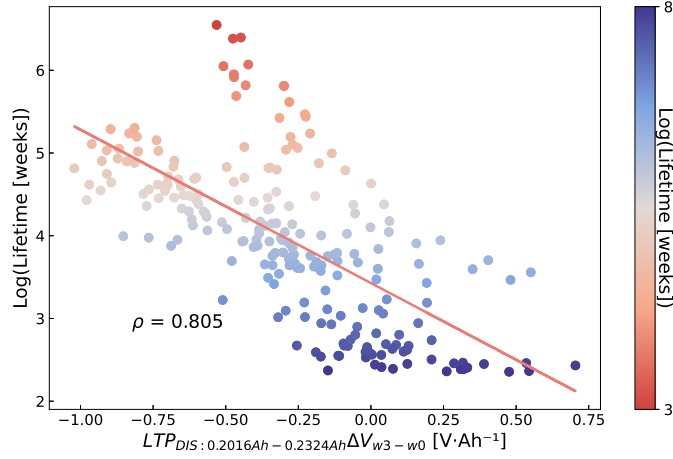
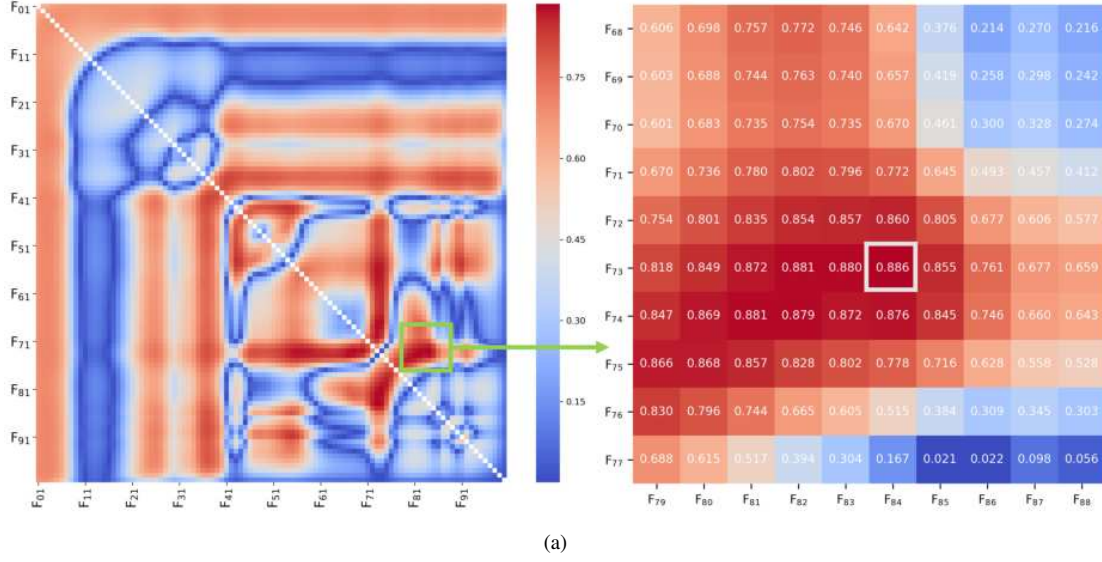


Figure 6: (a) Selection of the BTPF using the Pearson correlation coefficient between each candidate two-point feature and the week life of 116 cells in the training set. F01 to F100 represent 100 values of discharge capacity from 0 Ah to 0.28 Ah at intervals of 2.8 mAh. The colors are determined based on the Pearson correlation coefficient values. (b) Week life of all 225 cells in Dataset 2 plotted as a function of $PTP_{DIS:0.2016Ah-0.2324Ah} \triangle V_{w3-w0}/dQ(Q)$, with a Pearson correlation coefficient of 0.805. The colors are determined based on the week life of cells.

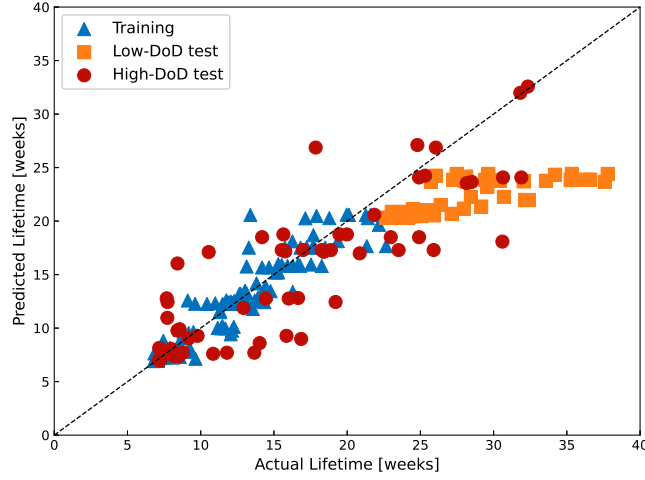


Figure 7: Week life prediction results of $PTP_{DIS:0.2016Ah-0.2324Ah} \triangle dV_{w3-w0}/dQ(Q)$ on 225 cells in Dataset 2. The input of XGBoost regression model is $PTP_{DIS:0.2016Ah-0.2324Ah} \triangle dV_{w3-w0}/dQ(Q)$, and the output is the cell week life.

4.2. Performance on the diagnosis task

4.2.1. Dataset 3

(1) BTPF extraction from EIS data

For Dataset 3, the BTPF extraction method for diagnosis task is shown in **Supplementary Figure 14**. To make a fair comparison with SOAT features [raw EIS impedances + future protocols] proposed by Jones et al. [46], this paper uses the same training and test sets as [46]. Specifically, Dataset 3 contains 88 commercial Li-ion coin cells with nominal capacities of 35 mAh (40 cells) and 40 mAh (48 cells). The sub-dataset 1 containing 40 commercial Li-ion coin cells with nominal capacity of 35 mAh is divided into a training set and a primary test set. The training set contains all 24 cells with variable discharge, and the primary test set contains all 16 cells with fixed discharge. Then, the sub-dataset 2 containing 48 commercial Li-ion coin cells with nominal capacity of 40 mAh is divided into a secondary test set and a third test set. The secondary test set contains all 32 cells cycled at the temperature of $23 \pm 2^\circ\text{C}$, and the third test set contains all 16 cells cycled at the temperature of $35 \pm 1^\circ\text{C}$. The training set is utilized to train the ML regression model, and the test sets are utilized to verify and test the estimation performance

of the trained ML regression model. To be consistent with [46], we first trained the ML regression model with the training set (24 cells) and tested it with the primary test set (16 cells). Then, we test the BTPF extraction method by using the secondary test set (32 cells). Here we assess how the ML regression model performs under 16-split validations, where two cells are randomly held out in each split. The final results are the average of the results obtained from 16-split validations. After that, we test the BTPF extraction method by using the third test set (16 cells). The ML regression model is trained on the secondary test set and tested on the third test set. For more details about the training and test sets, please refer to [46] and will not be repeated here.

Data collection: We collect the EIS data after full discharge in each cycle (a total of 114 real and imaginary impedances corresponding to 57 frequencies between 0.02Hz and 20kHz) for feature extraction.

Difference calculation: We subtract the real impedance vs. frequency (Re/f) data and imaginary impedance vs. frequency (Im/f) data collected in the first cycle from the corresponding data in higher cycles to obtain the $\Delta Re_{n-1}/f$ and $\Delta Im_{n-1}/f$ curves respectively. It should be noted here that since the frequency of EIS data collection in each cycle is the same, there is no need to perform spline function fitting and unified linear interpolation like Dataset 1 and Dataset 2. Instead, the $\Delta Re_{n-1}/f$ and $\Delta Im_{n-1}/f$ curves can be obtained by directly subtracting the EIS data in the first cycle from the EIS data in higher cycles. As shown in **Supplementary Figures 15(a) and 15(b)**, the obtained $\Delta Re_{10-1}/f$ and $\Delta Im_{10-1}/f$ curves are the shaded parts between the two Re/f curves and the two Im/f curves in the 1st and 10th cycles, respectively. The $\Delta Re_{n-1}/f$ and $\Delta Im_{n-1}/f$ curves of the representative cell in Dataset 3 are provided in **Supplementary Figures 15(c) and 15(d)**.

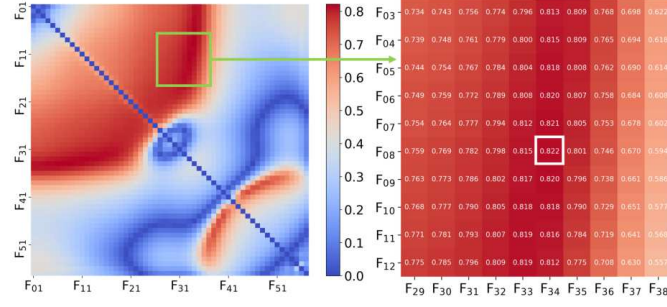
Feature extraction: The real impedance difference (ΔRe) values corresponding to any two frequency values on the $\Delta Re_{n-1}/f$ curve are subtracted and the absolute value is taken as a candidate two-point feature, as shown in **Supplementary Figure 16(a)**. Since the frequency is divided into 57 values between 0.02Hz and 20kHz during EIS measurement, a total of $(57^2 - 57)/2 = 1596$ candidate two-point features

can be obtained by traversing all combinations of two frequency values on the $\Delta Re_{n-1}/f$ curve, as shown in Figure 8(a). Further, all candidate two-point features of all cells in the training set on the $\Delta Re_{n-1}/f$ curve are traversed. We can use the same method in **Supplementary Figure 16(b)** to obtain all candidate two-point features on the $\Delta Im_{n-1}/f$ curve of all cells in the training set, as shown in Figure 8(b).

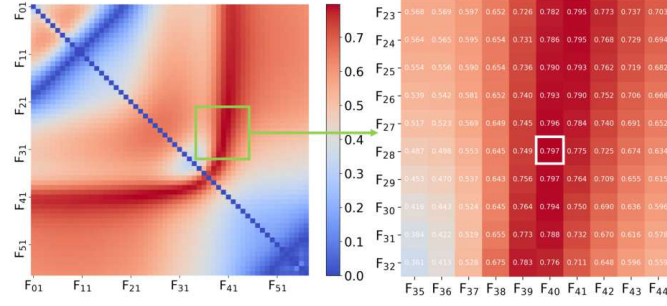
Feature selection: The Pearson correlation coefficient between each candidate two-point feature and capacities of 24 cells in the training set is calculated, and the candidate two-point feature corresponding to the correlation coefficient with the largest absolute value of 0.822 is selected as the BTPF $DT P_{ADIS:1922.08Hz-4.36Hz} \Delta Re_{n-1}/f(f)$ on the $\Delta Re_{n-1}/f$ curve, as shown in Figure 8(a). The two data points on the $\Delta Re_{n-1}/f$ curve that utilized to calculate $DT P_{ADIS:1922.08Hz-4.36Hz} \Delta Re_{n-1}/f(f)$ are shown in **Supplementary Figure 15(c)**. Similarly, the BTPF $DT P_{ADIS:17.79Hz-1.07Hz} \Delta Im_{n-1}/f(f)$ on the $\Delta Im_{n-1}/f$ curve is selected, and the corresponding Pearson correlation coefficient is 0.797, as shown in Figure 8(b). The two data points on the $\Delta Im_{n-1}/f$ curve that utilized to calculate $DT P_{ADIS:17.79Hz-1.07Hz} \Delta Im_{n-1}/f(f)$ are shown in **Supplementary Figure 15(d)**. The distribution relationship between capacities of all 40 cells in the sub-dataset 1 of Dataset 3 and the BTPFs ($DT P_{ADIS:1922.08Hz-4.36Hz} \Delta Re_{n-1}/f(f)$ and $DT P_{ADIS:17.79Hz-1.07Hz} \Delta Im_{n-1}/f(f)$) is shown in Figures 8(c) and 8(d). The Pearson correlation coefficients are 0.815 and 0.782, respectively.

SoH estimation: Since the Pearson correlation coefficient corresponding to $DT P_{ADIS:1922.08Hz-4.36Hz} \Delta Re_{n-1}/f(f)$ is greater than that of $DT P_{ADIS:17.79Hz-1.07Hz} \Delta Im_{n-1}/f(f)$, this paper selects $DT P_{ADIS:1922.08Hz-4.36Hz} \Delta Re_{n-1}/f(f)$ for ML regression model training and testing. Combining the BTPF $DT P_{ADIS:1922.08Hz-4.36Hz} \Delta Re_{n-1}/f(f)$ and the XGBoost regression model, the cell SoH estimation results are shown in Figure 9(a). The input of the XGBoost regression model is $DT P_{ADIS:1922.08Hz-4.36Hz} \Delta Re_{n-1}/f(f)$, and the output is the cell capacity. Combining the raw EIS impedance features [46] and the XGBoost regression model, the cell SoH estimation results are shown in Figure 9(b). The input of the XGBoost regression model is 114 raw EIS impedances, and the output is the cell capacity.

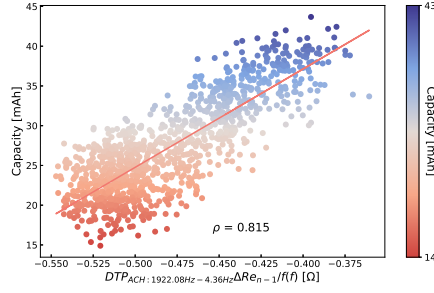
SoH estimation results of different features on the training set and primary test set in Dataset 3 are



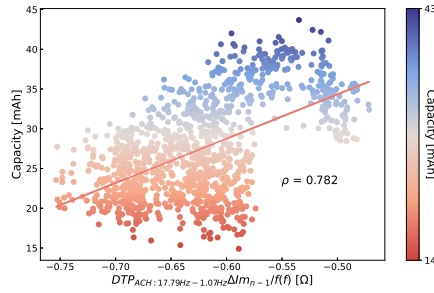
(a)



(b)

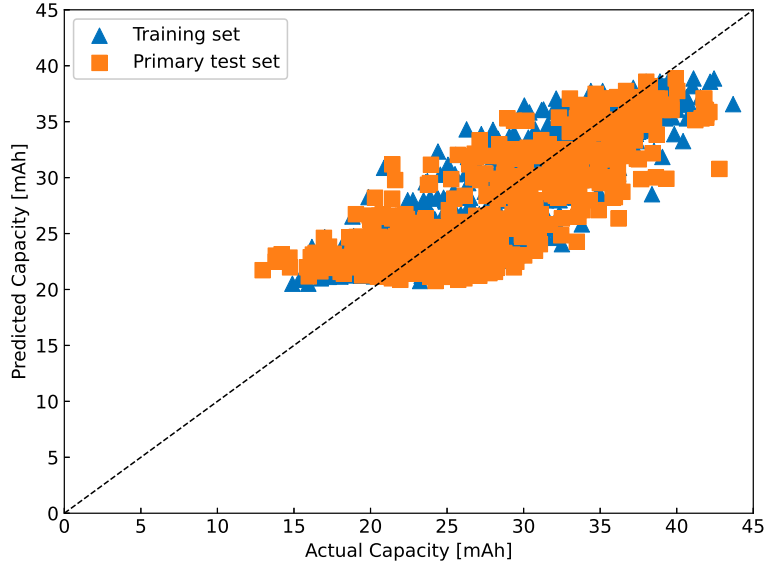


(c)

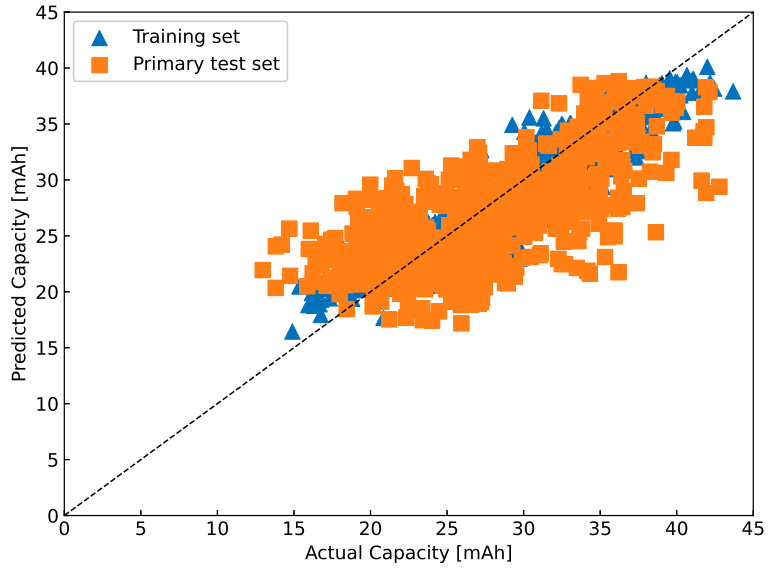


(d)

Figure 8: (a) Selection of the BTPF on the $\Delta Re_{n-1}/f$ curve using the Pearson correlation coefficient between each candidate two-point feature and capacities of 24 cells in the training set. F01 to F57 represent 57 frequencies from 0.02Hz to 20kHz. The colors are determined based on the Pearson correlation coefficient values. (b) Selection of the BTPF on the $\Delta Im_{n-1}/f$ curve using the Pearson correlation coefficient between each candidate two-point feature and capacities of 24 cells in the training set. F01 to F57 represent 57 frequencies from 0.02Hz to 20kHz. The colors are determined based on the Pearson correlation coefficient values. (c) Capacities plotted as a function of $DTP_{ADIS:1922.08Hz-4.36Hz} \Delta Re_{n-1}/f(f)$, with a Pearson correlation coefficient of 0.815. The colors are determined based on the capacities of cells. (d) Capacities plotted as a function of $DTP_{ADIS:17.79Hz-1.07Hz} \Delta Im_{n-1}/f(f)$, with a Pearson correlation coefficient of 0.782. The colors are determined based on the capacities of cells.



(a)



(b)

Figure 9: SoH estimation results of different features on 40 cells in the sub-dataset 1 of Dataset 3. (a) SoH estimation results of $DTP_{ADIS:1922.08Hz-4.36Hz} \triangle Re_{n-1}/f(f)$. The input of the XGBoost regression model is $DTP_{ADIS:1922.08Hz-4.36Hz} \triangle Re_{n-1}/f(f)$, and the output is the cell capacity. (b) SoH estimation results of raw EIS impedance features [46]. The input of the XGBoost regression model is 114 raw EIS impedances, and the output is the cell capacity.

shown in Table 3. More detailed results are shown in **Supplementary Tables 15 and 16**. It can be found that $DT P_{ADIS:1922.08Hz-4.36Hz} \triangle Re_{n-1}/f(f)$ achieves a comparable accuracy to that of raw EIS impedance features [46], while the raw EIS impedance features use 114 impedance data points, which is 57 times that of $DT P_{ADIS:1922.08Hz-4.36Hz} \triangle Re_{n-1}/f(f)$. Fewer data points mean less data collection, storage, and computational costs.

Furthermore, combining the BTPF $DT P_{ADIS:1922.08Hz-4.36Hz} \triangle Re_{n-1}/f(f)$ with the future cycling protocol feature proposed in [46] (including two current values of two-stage CC charging protocol and one current value of single stage CC discharge protocol), the SoH estimation results on the sub-dataset 1 of Dataset 3 are shown in **Supplementary Figure 17(a)**. Combining the raw EIS impedance features with the future cycling protocol feature, the SoH estimation results are shown in **Supplementary Figure 17(b)**. After combining different features with the future cycling protocol feature, the SoH estimation results on sub-dataset 1 of Dataset 3 are shown in **Supplementary Tables 17 and 18**. It can be found that after combining with the future cycling protocol feature, $DT P_{ADIS:1922.08Hz-4.36Hz} \triangle Re_{n-1}/f(f)$ achieves a comparable accuracy to that of raw EIS impedance features [46].

Moreover, based on 48 cells in the sub-dataset 2 of Dataset 3, the generalizability of the proposed BTPF extraction method is tested. For the secondary test set containing 32 cells cycled at the temperature of $23 \pm 2^\circ C$, the test results are shown in **Supplementary Figures 18 to 19** and **Supplementary Tables 19 to 20**. For the third test set containing 16 cells cycled at the temperature of $35 \pm 1^\circ C$, the test results are shown in **Supplementary Figures 20 to 21** and **Supplementary Tables 21 to 22**.

(2) BTPF extraction from DRT data

Similar to the BTPF extracted from the EIS data (**Supplementary Figure 14**), we also can extract the BTPF from the DRT data, as shown in **Supplementary Figure 22**.

Data collection: By using the open-source software pyDRTtools [75], we convert the EIS data after full discharge in each cycle (114 real and imaginary impedances corresponding to 57 frequencies between 0.02Hz and 20kHz) to DRT ($\gamma(\tau)/\tau$) data for feature extraction, where $\gamma(\tau)$ is the actual DRT and τ is

the time.

Difference calculation: We subtract the DRT data collected in the first cycle from the corresponding data in higher cycles to obtain the $\Delta\gamma(\tau)_{n-1}/\tau$ curve. It should be noted here that since the time of DRT data calculated in each cycle is the same, there is no need to perform spline function fitting and unified linear interpolation like Dataset 1 and Dataset 2. Instead, the $\Delta\gamma(\tau)_{n-1}/\tau$ curve can be obtained by directly subtracting the DRT data in the first cycle from the DRT data in higher cycles. As shown in **Supplementary Figure 23(a)**, the obtained $\Delta\gamma(\tau)_{10-1}/\tau$ curve is the shaded parts between the two $\gamma(\tau)/\tau$ curves in the 1st and 10th cycles. The $\Delta\gamma(\tau)_{n-1}/\tau$ curve in all cycles of the representative cell in Dataset 3 are provided in **Supplementary Figure 23(b)**.

Feature extraction: The $\Delta\gamma(\tau)$ values corresponding to any two time values on the $\Delta\gamma(\tau)_{n-1}/\tau$ curve are subtracted and the absolute value is taken as a candidate two-point feature, as shown in **Supplementary Figure 24**. Since the time is divided into 570 values between $3.19e^{-5}s$ and $1.18e^2s$ during DRT data calculation, a total of $(570^2 - 570)/2 = 162165$ candidate two-point features can be obtained by traversing all combinations of two timescale values on the $\Delta\gamma(\tau)_{n-1}/\tau$ curve. To reduce the computational burden, we only sample 1 time data point from every 10 time data points to extract candidate two-point features. Then, a total of $(57^2 - 57)/2 = 1596$ candidate two-point features can be obtained by traversing all combinations of two time values. Increasing the time interval does not affect the fairness of the comparison. Further, all candidate two-point features on the $\Delta\gamma(\tau)_{n-1}/\tau$ curve of all cells in the training set are traversed.

Feature selection: The Pearson correlation coefficient between each candidate two-point feature on the $\Delta\gamma(\tau)_{n-1}/\tau$ curve and capacities of all 24 cells in the training set is calculated, and the candidate two-point feature corresponding to the correlation coefficient with the largest absolute value of 0.785 is selected as the BTPF $DTP_{ADIS:1.23e^{-4}-5.41e^{-3}} \Delta\gamma(\tau)_{n-1}/\tau$, as shown in Figure 10(a). The two data points on the $\Delta\gamma(\tau)_{n-1}/\tau$ curve that utilized to calculate $DTP_{ADIS:1.23e^{-4}-5.41e^{-3}} \Delta\gamma(\tau)_{n-1}/\tau$ are shown in **Supplementary Figure 23(b)**. The distribution relationship between capacities of 40 cells in Subdataset

1 and the BTPF $DTP_{ADIS:1.23e-4-5.41e-3} \triangle \gamma(\tau)_{n-1}/\tau$ is shown in Figure 10(b). The Pearson correlation coefficient is 0.773.

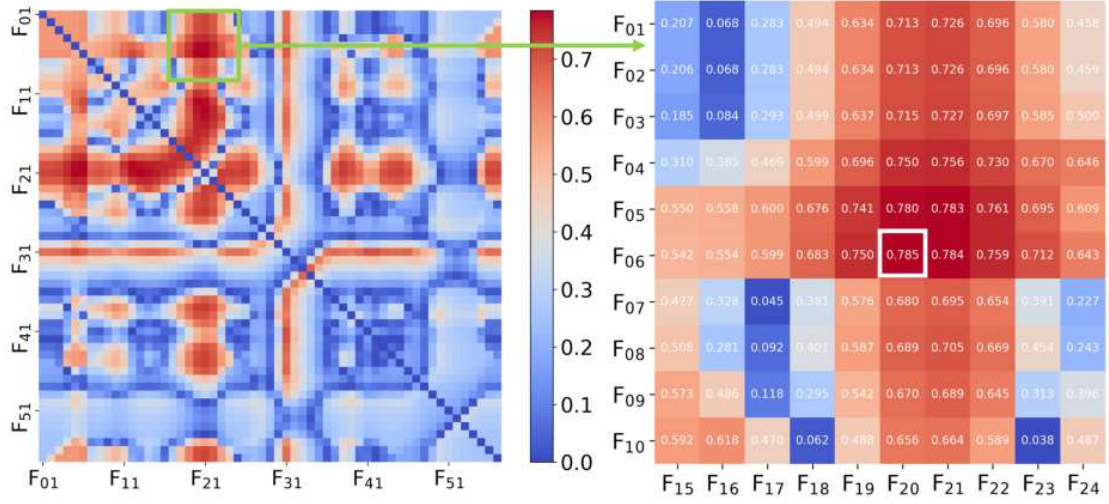
SoH estimation: Combining the BTPF $DTP_{ADIS:1.23e-4-5.41e-3} \triangle \gamma(\tau)_{n-1}/\tau$ and the XGBoost regression model, the battery SoH estimation results are shown in Figure 11(a). Furthermore, combining the BTPF $DTP_{ADIS:1.23e-4-5.41e-3} \triangle \gamma(\tau)_{n-1}/\tau$ with the future cycling protocol features [46], the battery SoH estimation results of the XGBoost regression model are shown in Figure 11(b). The battery SoH estimation results of different features on Subdataset 1 of Dataset 3 are shown in Table 3. More detailed results are shown in **Supplementary Tables 23 and 24**. It can be found that $DTP_{ADIS:1.23e-4-5.41e-3} \triangle \gamma(\tau)_{n-1}/\tau$ achieves a comparable accuracy to that of raw EIS impedance features [46].

4.2.2. Dataset 4

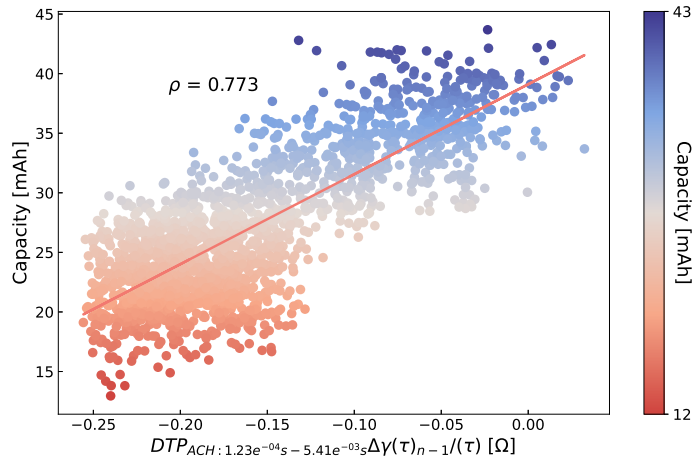
(1) BTPF extraction from EIS data

For Dataset 4, the BTPF extraction method for diagnosis task is exactly the same as Dataset 3, as shown in **Supplementary Figure 14**. To make a fair comparison with SOAT features (raw EIS impedances) proposed by Zhang et al. [49], this paper uses the same training and test sets as [49]. Specifically, Dataset 4 containing 12 commercial Li-ion coin cells with a nominal capacity of 45 mAh is divided into a training set and a test set. The training set (25C01–25C04, 35C01, and 45C01) and the test set (25C05–25C08, 35C02, and 45C02) both contain 6 cells. The training set is utilized to train the ML regression model, and the test set is utilized to verify and test the estimation performance of the trained ML regression model. To be consistent with [49], we first trained the ML regression model with four cells in the training set (25C01–25C04) and tested it with four cells in the test set (25C05–25C08). Then, we trained the ML regression model with all cells in the training set and tested it with all cells in the test set. For more details about the training and test sets, please refer to [49] and will not be repeated here.

Data collection: We collect the EIS data after full charge in each cycle (a total of 120 real and imaginary impedances corresponding to 60 frequencies between 0.02Hz and 20kHz) for feature extraction.

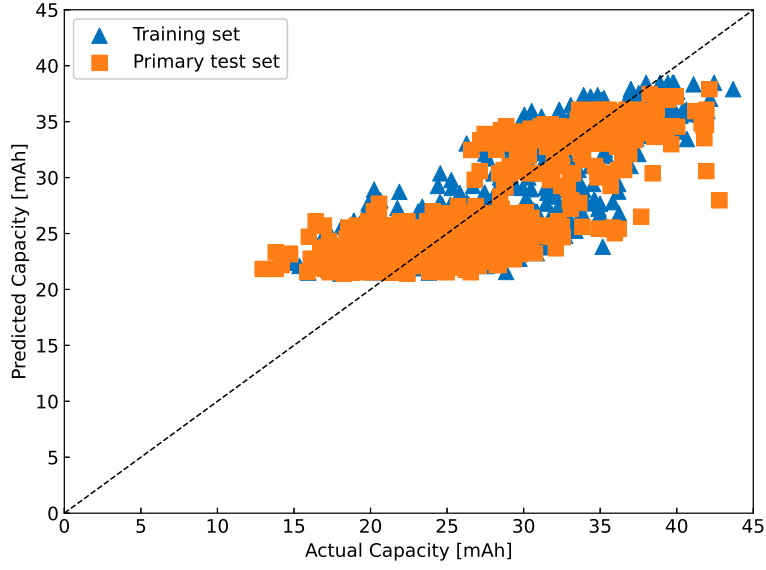


(a)

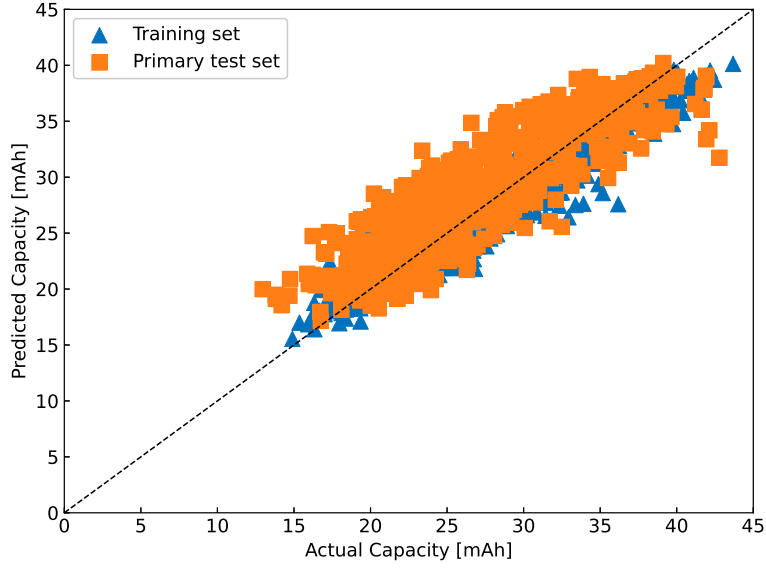


(b)

Figure 10: (a) Selection of the BTPF on the $\Delta \gamma(\tau)_{n-1}/\tau$ curve using the Pearson correlation coefficient between each candidate two-point feature and capacities of 24 cells in the training set. F01 to F57 represent 57 time values between $3.19e^{-5}s$ and $1.18e^2s$. The colors are determined based on the Pearson correlation coefficient values. (b) Capacities of 40 cells in Subdataset 1 plotted as functions of $DTP_{ADIS:1.23e^{-4}s-5.41e^{-3}s} \Delta \gamma(\tau)_{n-1}/\tau$. The colors are determined based on the capacities of cells.



(a)



(b)

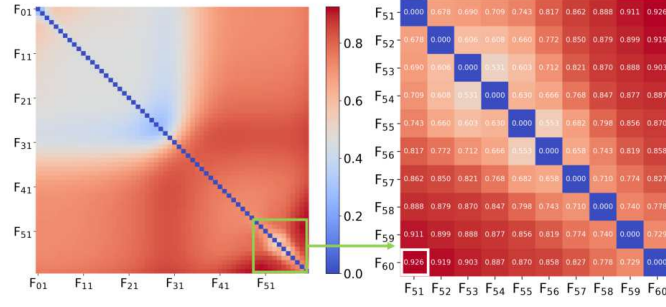
Figure 11: SoH estimation results of different features on the sub-dataset 1 of Dataset 3 (40 cells). (a) SoH estimation results of $DTP_{ADIS:1.23e-4-5.41e-3} \triangle \gamma(\tau)_{n-1}/\tau$. The input of the XGBoost regression model is $DTP_{ADIS:1.23e-4-5.41e-3} \triangle \gamma(\tau)_{n-1}/\tau$, and the output is the cell capacity. (b) SoH estimation results of features $[DTP_{ADIS:1.23e-4-5.41e-3} \triangle \gamma(\tau)_{n-1}/\tau, \text{future protocols}]$. The input of the XGBoost regression model is $DTP_{ADIS:1.23e-4-5.41e-3} \triangle \gamma(\tau)_{n-1}/\tau$ and the future cycling protocol features, and the output is the cell capacity.

Difference calculation: We subtract the Re/f data and Im/f data collected in the first cycle from the corresponding data in higher cycles to obtain the $\Delta Re_{n-1}/f$ and $\Delta Im_{n-1}/f$ curves respectively, as shown in **Supplementary Figures 25(a) and 25(b)**. The $\Delta Re_{n-1}/f$ and $\Delta Im_{n-1}/f$ curves of the representative cell in Dataset 4 are provided in **Supplementary Figures 25(c) and 25(d)**.

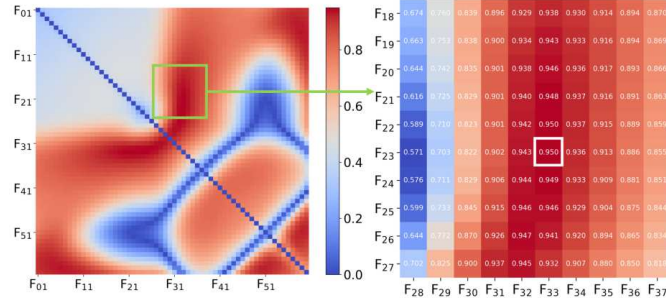
Feature extraction: The real impedance difference (ΔRe) values corresponding to any two frequency values on the $\Delta Re_{n-1}/f$ curve are subtracted and the absolute value is taken as a candidate two-point feature, as shown in **Supplementary Figure 16(a)**. Since the frequency is divided into 60 values between 0.02Hz and 20kHz during EIS measurement, a total of $(60^2 - 60)/2 = 1770$ candidate two-point features can be obtained by traversing all combinations of two frequency values on the $\Delta Re_{n-1}/f$ curve, as shown in Figure 12(a). Further, all candidate two-point features of all cells in the training set on the $\Delta Re_{n-1}/f$ curve are traversed. We can use the same method in **Supplementary Figure 16(b)** to obtain all candidate two-point features on the $\Delta Im_{n-1}/f$ curve of all cells in the training set, as shown in Figure 12(b).

Feature selection: The Pearson correlation coefficient between each candidate two-point feature and capacities of 4 cells in the training set (25C01–25C04) is calculated, and the candidate two-point feature corresponding to the correlation coefficient with the largest absolute value of 0.926 is selected as the BTPF $DTP_{ACH:0.165Hz-0.019Hz} \Delta Re_{n-1}/f(f)$ of the $\Delta Re_{n-1}/f$ curve, as shown in Figure 12(a). The two data points on the $\Delta Re_{n-1}/f$ curve that utilized to calculate $DTP_{ACH:0.165Hz-0.019Hz} \Delta Re_{n-1}/f(f)$ are shown in **Supplementary Figure 25(c)**. Similarly, the BTPF $DTP_{ACH:115.778Hz-11.145Hz} \Delta Im_{n-1}/f(f)$ of the $\Delta Im_{n-1}/f$ curve is selected, and the corresponding Pearson correlation coefficient is 0.950, as shown in Figure 12(b). The two data points on the $\Delta Im_{n-1}/f$ curve that utilized to calculate $DTP_{ACH:115.778Hz-11.145Hz} \Delta Im_{n-1}/f(f)$ are shown in **Supplementary Figure 25(d)**. The distribution relationship between capacities of 8 cells in Dataset 4 (25C01–25C08) and the BTPFs ($DTP_{ACH:0.165Hz-0.019Hz} \Delta Re_{n-1}/f(f)$ and $DTP_{ACH:115.778Hz-11.145Hz} \Delta Im_{n-1}/f(f)$) is shown in Figures 12(c) and 12(d). The Pearson correlation coefficients are 0.892 and 0.924, respectively.

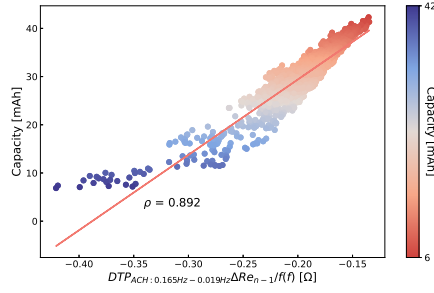
SoH estimation: Since the Pearson correlation coefficient corresponding to $DTP_{ACH:0.165Hz-0.019Hz} \Delta$



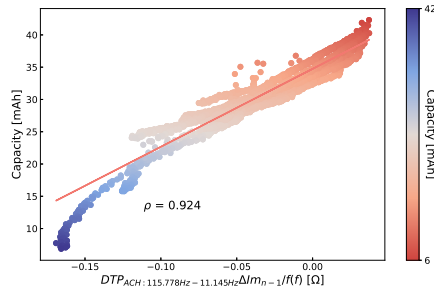
(a)



(b)



(c)



(d)

Figure 12: Selection of the BTPF using the Pearson correlation coefficient between each candidate two-point feature and capacities of 4 cells in the training set (25C01–25C04). F01 to F60 represent 60 frequencies from 0.02Hz to 20kHz. The colors are determined based on the Pearson correlation coefficient values. (a) Selection of the BTPF on the $\Delta Re_{n-1}/f$ curve using the Pearson correlation coefficient between each candidate two-point feature and capacities of 4 cells in the training set (25C01–25C04). F01 to F60 represent 60 frequencies from 0.02Hz to 20kHz. The colors are determined based on the Pearson correlation coefficient values. (b) Selection of the BTPF on the $\Delta Im_{n-1}/f$ curve using the Pearson correlation coefficient between each candidate two-point feature and capacities of 4 cells in the training set (25C01–25C04). F01 to F60 represent 60 frequencies from 0.02Hz to 20kHz. The colors are determined based on the Pearson correlation coefficient values. (c) Capacities 8 cells in Dataset 4 (25C01–25C08) plotted as a function of $DTP_{ACH:f1-f2} \Delta Re_{n-1}/f(f)$, with a Pearson correlation coefficient of 0.892. The colors are determined based on the capacities of cells. (d) Capacities plotted as a function of $DTP_{ACH:f1-f2} \Delta Im_{n-1}/f(f)$, with a Pearson correlation coefficient of 0.924. The colors are determined based on the capacities of cells.

$Re_{n-1}/f(f)$ is less than that of $DTP_{ACH:115.778Hz-11.145Hz} \triangle Im_{n-1}/f(f)$, this paper selects $DTP_{ACH:115.778Hz-11.145Hz} \triangle Im_{n-1}/f(f)$ for ML regression model training and testing. Combining the BTPF $DTP_{ACH:115.778Hz-11.145Hz} \triangle Im_{n-1}/f(f)$ and the XGBoost regression model, the cell SoH estimation results are shown in Figure 13(a). Combining the raw EIS impedance features [49] and the XGBoost regression model, the cell SoH estimation results are shown in Figure 13(b).

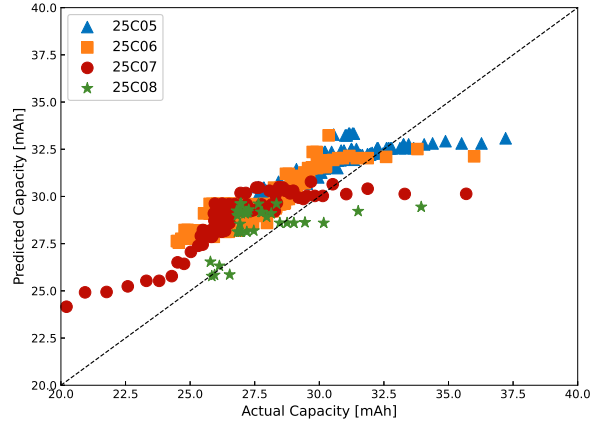
SoH estimation results of different features on 4 cells in Dataset 4 (25C05–25C08) are shown in Table 4. More detailed results are shown in **Supplementary Tables 25 to 28**. It can be found that $DTP_{ACH:115.778Hz-11.145Hz} \triangle Im_{n-1}/f(f)$ achieves a comparable accuracy to that of raw EIS impedance features [49], while the raw EIS impedance features use 120 impedance data points, which is 60 times that of $DTP_{ACH:115.778Hz-11.145Hz} \triangle Im_{n-1}/f(f)$. Fewer data points mean less data collection, storage, and computational costs.

Zhang et al. [49] determined the importance weights of raw EIS impedances at different frequencies through the ARD of the GPR model, and found that the two imaginary impedances, corresponding to 17.80 Hz and 2.16 Hz, have more significant importance weights than other impedances, and the use of these two imaginary impedances can accurately estimate the SoH of the cell. Furthermore, we compare the BTPF $DTP_{ACH:115.778Hz-11.145Hz} \triangle Im_{n-1}/f(f)$ proposed in this paper with the two imaginary impedance features proposed in [49], and the SoH estimation results are shown in Figure 12(c) and **Supplementary Tables 25 to 28**. It can be found that $DTP_{ACH:115.778Hz-11.145Hz} \triangle Im_{n-1}/f(f)$ achieves more accurate SoH estimation results than two imaginary impedance features [49].

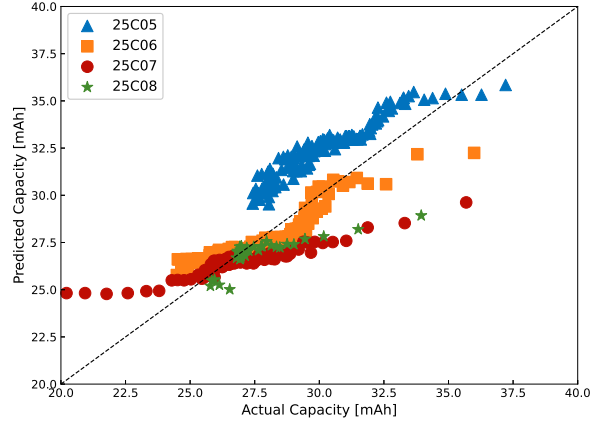
Furthermore, we trained the ML regression model with all 6 cells in the training set and tested it with all 6 cells in the test set, SoH estimation results of different features on cells 35C02 and 45C02 are shown in **Supplementary Figure 26** and **Supplementary Tables 29 to 30**.

(2) BTPF extraction from DRT data

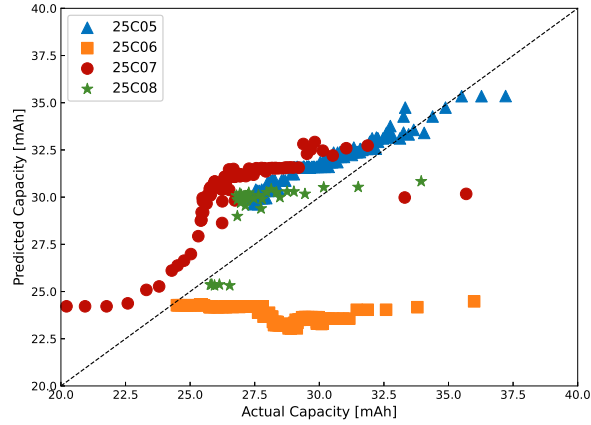
We can also extract the BTPF from the DRT data, which is exactly the same as Dataset 3, as shown in **Supplementary Figure 22**.



(a)



(b)



(c)

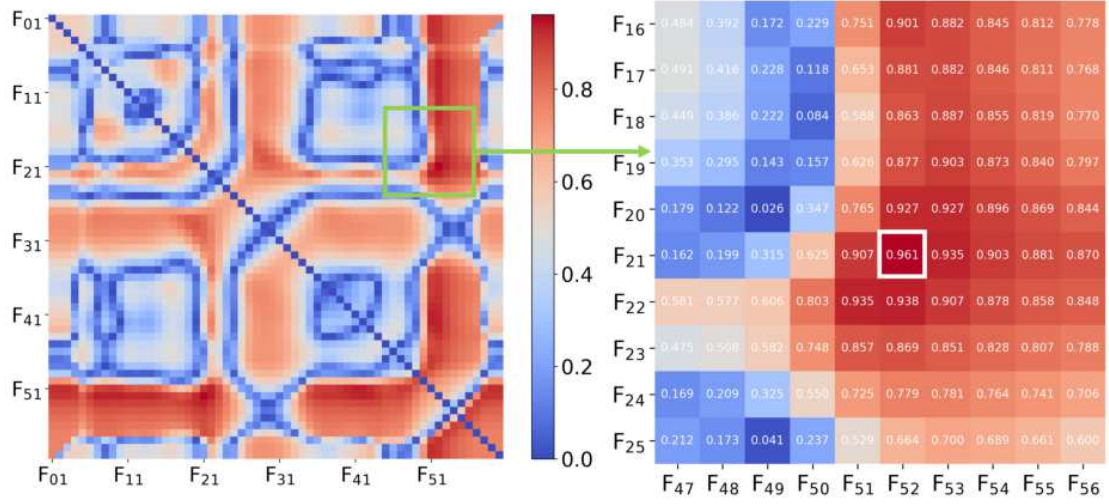
Figure 13: SoH estimation results of different features on 8 cells in Dataset 4 (25C01–25C08). (a) SoH estimation results of $DTP_{ACH:115.778Hz-11.145Hz} \triangle Im_{n-1}/f(f)$. The input of the XGBoost regression model is $DTP_{ACH:115.778Hz-11.145Hz} \triangle Im_{n-1}/f(f)$, and the output is the cell capacity. (b) SoH estimation results of raw EIS impedance features [49]. The inputs of the XGBoost regression model are 120 raw EIS impedances, and the output is the cell capacity. (c) SoH estimation results of two imaginary impedance features corresponding to 17.80 Hz and 2.16 Hz. The inputs of the XGBoost regression model are two imaginary impedances corresponding to 17.80 Hz and 2.16 Hz, and the output is the cell capacity.

Data collection: By using the open-source software pyDRTtools [75], We convert the EIS data after full charge in each cycle (120 real and imaginary impedances corresponding to 60 frequencies between 0.02Hz and 20kHz) to DRT ($\gamma(\tau)/\tau$) data for feature extraction.

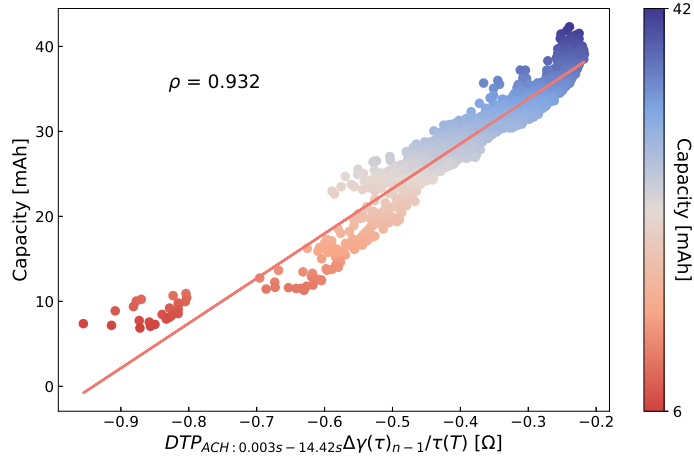
Difference calculation: We subtract the DRT data collected in the first cycle from the corresponding data in higher cycles to obtain the $\Delta\gamma(\tau)_{n-1}/\tau$ curve, as shown in **Supplementary Figure 27(a)**. The $\Delta\gamma(\tau)_{n-1}/\tau$ curve in all cycles of the representative cell in Dataset 4 are provided in **Supplementary Figure 27(b)**.

Feature extraction: The $\Delta\gamma(\tau)$ values corresponding to any two time values on the $\Delta\gamma(\tau)_{n-1}/\tau$ curve are subtracted and the absolute value is taken as a candidate two-point feature, as shown in **Supplementary Figure 24**. Since the time is divided into 600 values between $1.58e^{-5}s$ and $1.24e^2s$ during DRT data calculation, a total of $(600^2 - 600)/2 = 179700$ candidate two-point features can be obtained by traversing all combinations of two timescale values on the $\Delta\gamma(\tau)_{n-1}/\tau$ curve. To reduce the computational burden, we only sample 1 time data point from every 10 time data points to extract candidate two-point features. Then, a total of $(60^2 - 60)/2 = 1770$ candidate two-point features can be obtained by traversing all combinations of two time values. Increasing the time interval does not affect the fairness of the comparison. Further, all candidate two-point features on the $\Delta\gamma(\tau)_{n-1}/\tau$ curve of 4 cells in the training set (25C01–25C04) are traversed, as shown in Figure 14(a).

Feature selection: The Pearson correlation coefficient between each candidate two-point feature on the $\Delta\gamma(\tau)_{n-1}/\tau$ curve and capacities of 4 cells in the training set (25C01–25C04) is calculated, and the candidate two-point feature corresponding to the correlation coefficient with the largest absolute value of 0.961 is selected as the BTPF $DTP_{ACH:0.003s-14.42s} \Delta\gamma(\tau)_{n-1}/\tau$ of the $\Delta\gamma(\tau)_{n-1}/\tau$ curve, as shown in Figure 14(a). The two data points on the $\Delta\gamma(\tau)_{n-1}/\tau$ curve that utilized to calculate $DTP_{ACH:0.003s-14.42s} \Delta\gamma(\tau)_{n-1}/\tau$ are shown in **Supplementary Figure 27(b)**. The distribution relationship between capacities of 8 cells in Dataset 4 (25C01–25C08) and the BTPF $DTP_{ACH:0.003s-14.42s} \Delta\gamma(\tau)_{n-1}/\tau$ is shown in Figure 14(b). The Pearson correlation coefficient is 0.932.



(a)



(b)

Figure 14: (a) Selection of the BTPF on the $\Delta\gamma(\tau)_{n-1}/\tau$ curve using the Pearson correlation coefficient between each candidate two-point feature and capacities of 4 cells in the training set (25C01–25C04). F01 to F60 represent 60 time values between $1.58e^{-5}s$ and $1.24e^2s$. The colors are determined based on the Pearson correlation coefficient values. (b) Capacities of 8 cells in Dataset 3 (25C01–25C08) plotted as functions of $DTP_{ACH:0.003s-14.42s} \Delta\gamma(\tau)_{n-1}/\tau$. The colors are determined based on the capacities of cells.

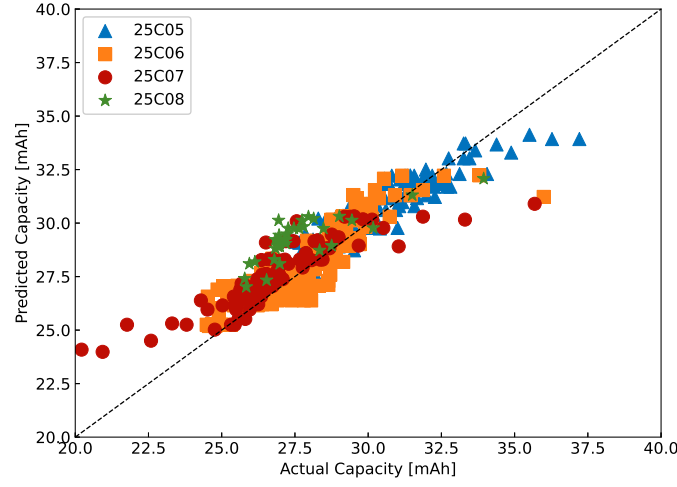


Figure 15: SoH estimation results of $DTP_{ACH:0.003s-14.42s} \triangle \gamma(\tau)_{n-1}/\tau$ on 8 cells in Dataset 4 (25C01–25C08). The input of the XGBoost regression model is $DTP_{ACH:0.003s-14.42s} \triangle \gamma(\tau)_{n-1}/\tau$, and the output is the cell capacity.

SoH estimation: Combining the BTPF $DTP_{ACH:0.003s-14.42s} \triangle \gamma(\tau)_{n-1}/\tau$ and the XGBoost regression model, the battery SoH estimation results of 8 cells in Dataset 3 (25C01–25C08) are shown in Figure 15.

SoH estimation results of $DTP_{ACH:0.003s-14.42s} \triangle \gamma(\tau)_{n-1}/\tau$ on 4 cells in the test set of Dataset 4 (25C05–25C08) are shown in Table 4. More detailed results are shown in **Supplementary Tables 31 to 34**. It can be found that $DTP_{ACH:0.003s-14.42s} \triangle \gamma(\tau)_{n-1}/\tau$ achieves a comparable accuracy to that of raw EIS impedance features and two imaginary impedance features [49].

4.2.3. Dataset 5

For Dataset 5, the BTPF extraction method for diagnosis task is shown in **Supplementary Figure 28**. To make a fair comparison with SOAT features [Variance, Skewness, Maximum] (abbreviated as [Var, Ske, Max]) proposed by Zhu et al. [45], this paper uses the same training set and test set as [45]. Specifically, the Dataset 5 containing 130 commercial Li-ion cells with different nominal capacities and chemistry types (66 NCA cells with nominal capacity of 3.5 Ah, 55 NCM cells with nominal capacity

of 3.5Ah, and 9 NCM+NCA cells with nominal capacity of 2.5 Ah) is divided into three sub-datasets, namely the sub-dataset 1 (66 NCA cells), the sub-dataset 2 (55 NCM cells), and the sub-dataset 3 (9 NCM+NCA cells). Among them, the sub-dataset 1 is divided into a training set (52 NCA cells) and a primary test set (14 NCA cells) by using a stratified sampling method, meaning that the data from the same cell is either in the training set or in the test set. The sub-dataset 2 is used as the secondary test set and the sub-dataset 3 is used as the third test set. To be consistent with [45], we first trained the ML regression model with the training set and tested it with the primary test set. Then, the ML regression model is trained on the sub-dataset 1 and tested on the secondary and third test sets. For more details about the training and test sets, please refer to [45] and will not be repeated here.

Data collection: We collect the relaxation V/t data within 1800s after full charge in each cycle. It should be noted here that in Dataset 5 [45], the 1800 s relaxation V/t data of NCA and NCM cells after full charge is collected at a sampling frequency of 120 s, and the 3600 s relaxation V/t data of NCM+NCA cells after full charge is collected at a sampling frequency of 30 s. Therefore, we selected the 1800 s relaxation V/t data after full charge for feature extraction.

Difference calculation: The relaxation V/t data collected in each cycle is standardized to facilitate subsequent calculations. Specifically, the spline function is utilized to fit the relaxation V/t data, and a unified linear interpolation is performed. The relaxation voltage is fitted as a function of the relaxation time, and the relaxation time linearly is divided into 50 values between 0s and 1800 s at intervals of 36 s, as shown in **Supplementary Figure 29(a)**. The fitted relaxation V/t data in the 1st cycle is subtracted from the fitted relaxation V/t data in the n th cycles to obtain the relaxation $\Delta V_{n-1}/t$ curve. As shown in **Supplementary Figure 29(b)**, the obtained relaxation $\Delta V_{n-1}/t$ curve is the shaded part between the two relaxation V/t curves in 1st and 10th cycles. The $\Delta V_{n-1}/t$ curves of the representative cell in Dataset 5 are provided in **Supplementary Figure 29(c)**.

Feature extraction: The relaxation ΔV values corresponding to any two relaxation time values on the $\Delta V_{n-1}/t$ curve are subtracted and the absolute value is taken as a candidate two-point feature, as

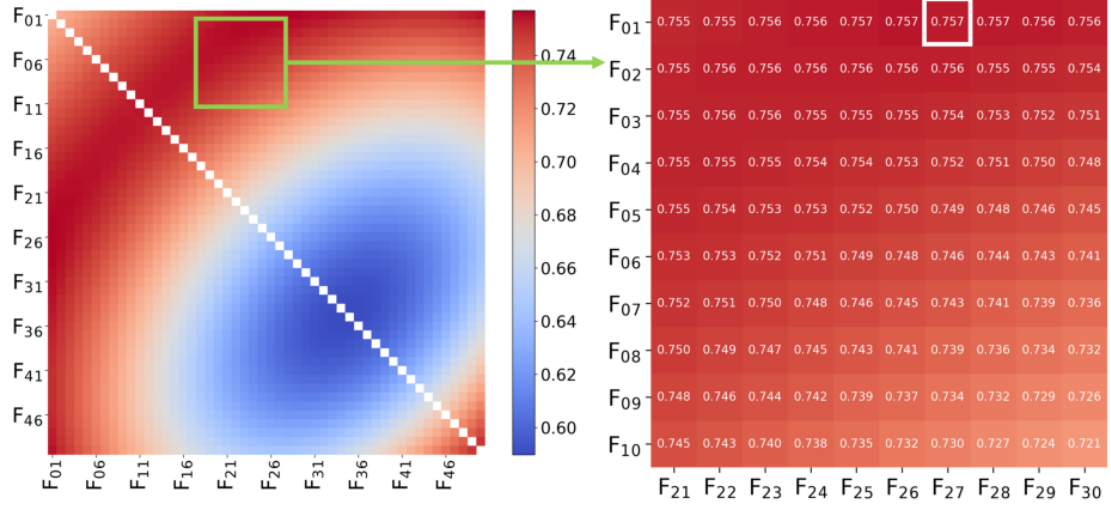
shown in **Supplementary Figure 30**. Since the relaxation time linearly is divided into 50 values between 0 s and 1800 s at intervals of 36 s, a total of $(50^2 - 50)/2 = 1225$ candidate two-point features can be obtained by traversing all combinations of two relaxation time values on the $\Delta V_{n-1}/t$ curve, as shown in Figure 16(a).

Feature selection: The Pearson correlation coefficient between each candidate two-point feature and capacities of 52 NCA cells in the training set is calculated, and the candidate two-point feature corresponding to the correlation coefficient with the largest absolute value of 0.757 is selected as the BTPF $DTP_{ACH:0s-936s} \Delta V_{n-1}/t(t)$ on the $\Delta V_{n-1}/t$ curve, as shown in Figure 16(a). The two data points on the $\Delta V_{n-1}/t$ curve that utilized to calculate $DTP_{ACH:0s-936s} \Delta V_{n-1}/t(t)$ are shown in **Supplementary Figure 29(c)**. The distribution relationship between capacities of 66 NCA cells in the sub-dataset 1 of Dataset 5 and the BTPF $DTP_{ACH:0s-936s} \Delta V_{n-1}/t(t)$ on the $\Delta V_{n-1}/t$ is shown in Figure 16(b). The Pearson correlation coefficient is 0.758.

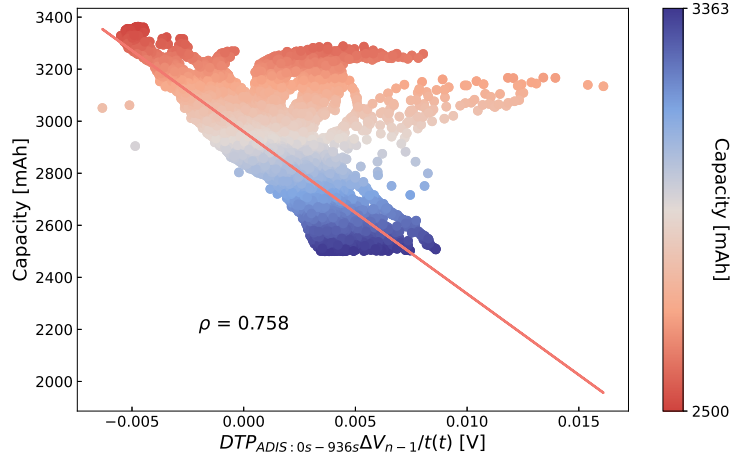
SoH estimation: Combining the BTPF $DTP_{ACH:0s-936s} \Delta V_{n-1}/t(t)$ and the XGBoost regression model, the battery SoH estimation results of the sub-dataset 1 in Dataset 5 (66 NCA cells) are shown in Figure 17(a). Combining the statistical features [Var, Ske, Max] proposed in [45] and the XGBoost regression model, the battery SoH estimation results of the sub-dataset 1 in Dataset 5 (66 NCA cells) are shown in Figure 17(b).

SoH estimation results of different features on the sub-dataset 1 of Dataset 5 (66 NCA cells) are shown in Table 5. More detailed results are shown in **Supplementary Tables 35 to 36**. It can be found that $DTP_{ACH:0s-936s} \Delta V_{n-1}/t(t)$ achieves a comparable accuracy to that of the statistical features [Var, Ske, Max] [45]. Compared with the statistical features [Var, Ske, Max], $DTP_{ACH:0s-936s} \Delta V_{n-1}/t(t)$ only needs to collect 2 data points from the relaxation V/t data in each cycle to calculate, while the statistical features [Var, Ske, Max] use 15 data points, which is 7.5 times that of $DTP_{ACH:0s-936s} \Delta V_{n-1}/t(t)$. Fewer data points mean less data collection, storage, and computing costs.

Moreover, based on 55 NCM cells in the secondary test set of Dataset 3, the generalizability of the

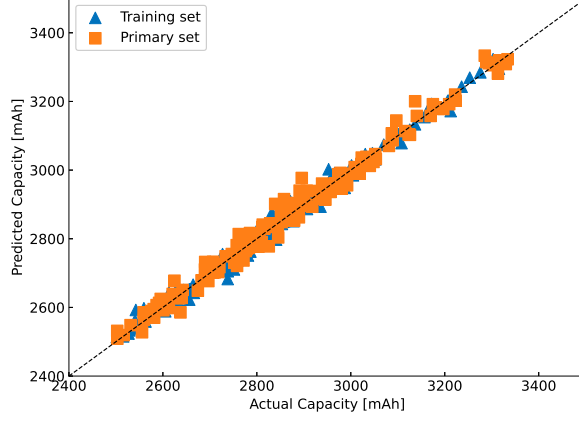


(a)

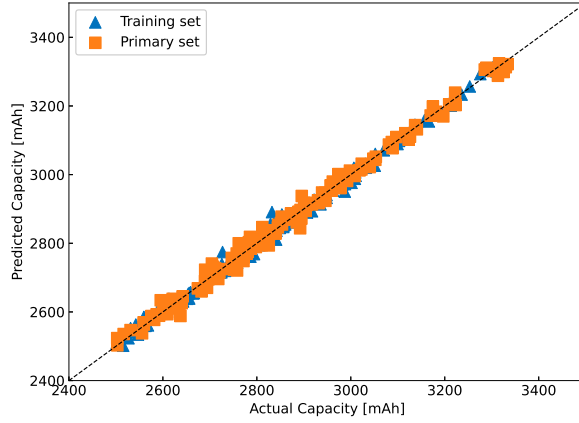


(b)

Figure 16: (a) Selection of the BTPF using the Pearson correlation coefficient between each candidate two-point feature and capacities of 52 NCA cells in the training set. F_{01} to F_{50} represent 50 relaxation time values between 0 s and 1800 s at intervals of 36 s. The colors are determined based on the Pearson correlation coefficient values. (b) Capacities of 66 NCA cells in the sub-dataset 1 of Dataset 5 plotted as a function of the BTPF $DTP_{ACH:0s-936s} \Delta V_{n-1}/t(t)$, with a Pearson correlation coefficient of 0.758.



(a)



(b)

Figure 17: SoH estimation results of different features on the sub-dataset 1 of Dataset 5 (66 NCA cells). (a) SoH estimation results of $DTP_{ACH:0s-936s} \triangle V_{n-1}/t(t)$. The input of the XGBoost regression model is $DTP_{ACH:0s-936s} \triangle V_{n-1}/t(t)$, and the output is the cell capacity. (b) SoH estimation results of statistical features [Var, Ske, Max] [45]. The inputs of the XGBoost regression model training are statistical features [Var, Ske, Max], and the output is the cell capacity.

proposed BTPF extraction method is tested, and the test results are shown in **Supplementary Figure 31**. More detailed test results are provided in **Supplementary Table 37**. Based on 9 NCM+NCA cells in the third test set of Dataset 3, the generalizability of the proposed BTPF extraction method is tested, and the test results are shown in **Supplementary Figure 32**. More detailed test results are provided in **Supplementary Table 38**.

4.2.4. Dataset 6

For Dataset 6, the BTPF extraction method for diagnosis task is exactly the same as Dataset 5, as shown in **Supplementary Figure 28**. Since Wildfeuer et al. [22] did not propose features for the battery diagnosis task when publishing the Dataset 6, we still use the SOAT features [Var, Ske, Max] proposed by Zhu et al. [45] to compare with the BTPF proposed in this paper. Specifically, Dataset 6 containing 196 commercial NCA cells with nominal capacities of 2.5 Ah is randomly divided into a training set and a test set, where 80% of the cells are randomly divided into the training set (157 cells) and 20% of the cells are divided into the test set (39 cells). The data of each cell is either in the training set or in the test set. We trained the ML regression model with the training set and tested it with the test set. For more details about Dataset 6, please refer to [22] and will not be repeated here.

Data collection: We collect the relaxation V/t data within 7200 s after full discharge in each periodic RPT.

Difference calculation: The relaxation V/t data collected in each RPT is standardized to facilitate subsequent calculations, as shown in **Supplementary Figure 33(a)**. The fitted relaxation V/t data in the 1st cycle is subtracted from the fitted relaxation V/t data in the n th cycles to obtain the relaxation $\Delta V_{n-1}/t$ curve, as shown in **Supplementary Figure 33(b)**. The $\Delta V_{n-1}/t$ curves of the representative cell in Dataset 6 are provided in **Supplementary Figure 33(c)**.

Feature extraction: The relaxation ΔV values corresponding to any two relaxation time values on the $\Delta V_{n-1}/t$ curve are subtracted and the absolute value is taken as a candidate two-point feature, as

shown in **Supplementary Figure 30**. Since the the relaxation time linearly is divided into 100 values between 0 s and 7200 s at intervals of 72 s, a total of $(100^2 - 100)/2 = 4950$ candidate two-point features can be obtained by traversing all combinations of two relaxation time values on the $\Delta V_{n-1}/t$ curve, as shown in Figure 18(a).

Feature selection: The Pearson correlation coefficient between each candidate two-point feature and capacities of 157 cells in the training set is calculated, and the candidate two-point feature corresponding to the correlation coefficient with the largest absolute value of 0.896 is selected as the BTPF $DTP_{ADIS:6120s-6984s} \triangle V_{n-1}/t(t)$ on the $\Delta V_{n-1}/t$ curve, as shown in Figure 18(a). The two data points on the $\Delta V_{n-1}/t$ curve that utilized to calculate $DTP_{ADIS:6120s-6984s} \triangle V_{n-1}/t(t)$ are shown in **Supplementary Figure 33(c)**. The distribution relationship between capacities of 196 cells in Dataset 6 and the BTPF $DTP_{ADIS:6120s-6984s} \triangle V_{n-1}/t(t)$ on the $\Delta V_{n-1}/t$ is shown in Figure 18(b). The Pearson correlation coefficient is 0.804.

SoH estimation: Combining the BTPF $DTP_{ADIS:6120s-6984s} \triangle V_{n-1}/t(t)$ and the XGBoost regression model, the battery SoH estimation results of 196 cells in Dataset 6 are shown in Figure 19(a). Combining the statistical features [Var, Ske, Max] proposed in [45] and the XGBoost regression model, the battery SoH estimation results of 196 cells in Dataset 6 are shown in Figure 19(b).

Figure 19 SoH estimation results of different features on 196 cells in Dataset 6. (a) SoH estimation results of $DTP_{ADIS:6120s-6984s} \triangle V_{n-1}/t(t)$. The input of the XGBoost regression model is $DTP_{ADIS:6120s-6984s} \triangle V_{n-1}/t(t)$, and the output is the cell capacity. (b) SoH estimation results of statistical features [Var, Ske, Max]. The input of the XGBoost regression model training is statistical features [Var, Ske, Max], and the output is the cell capacity.

SoH estimation results of different features on 196 cells of Dataset 6 are shown in Table 6. More detailed results are shown in **Supplementary Tables 39 to 40**. It can be found that $DTP_{ADIS:6120s-6984s} \triangle V_{n-1}/t(t)$ achieves a comparable accuracy to that of the statistical features [Var, Ske, Max], while the statistical features [Var, Ske, Max] use about 720 data points, which is 360 times that of $DTP_{ADIS:6120s-6984s} \triangle V_{n-1}/t(t)$.

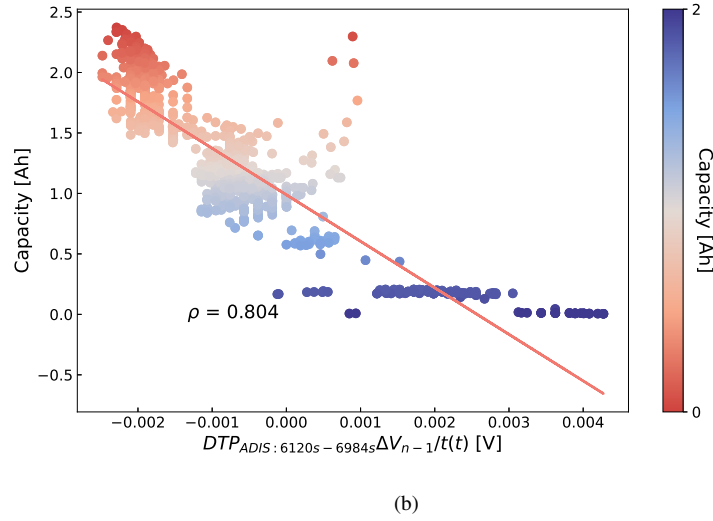
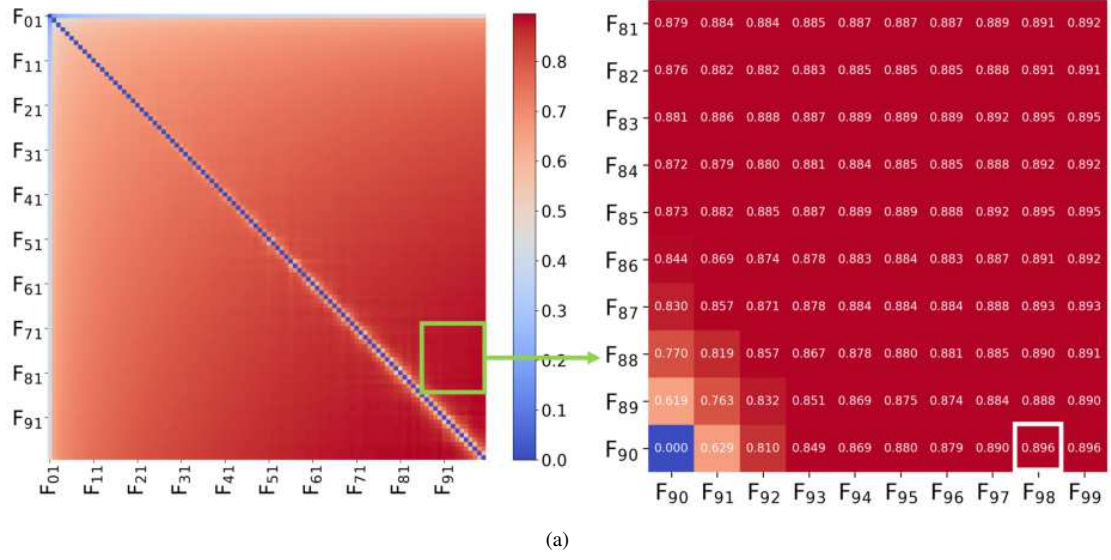
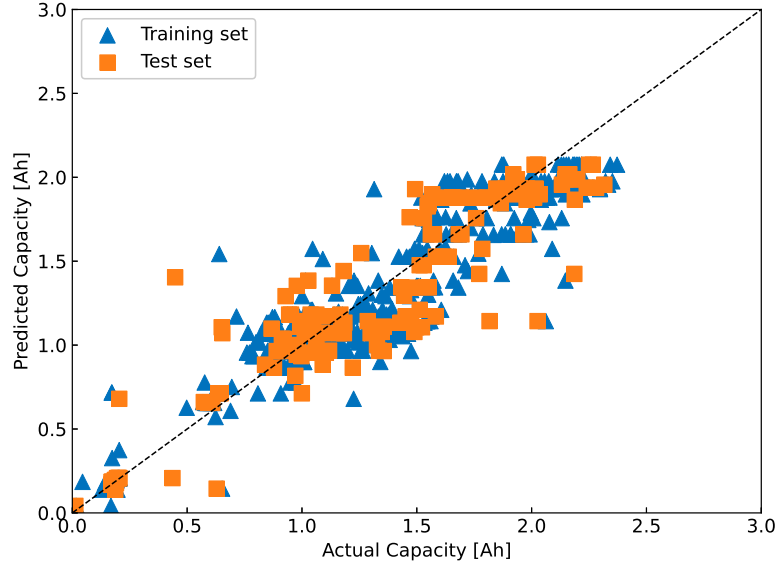
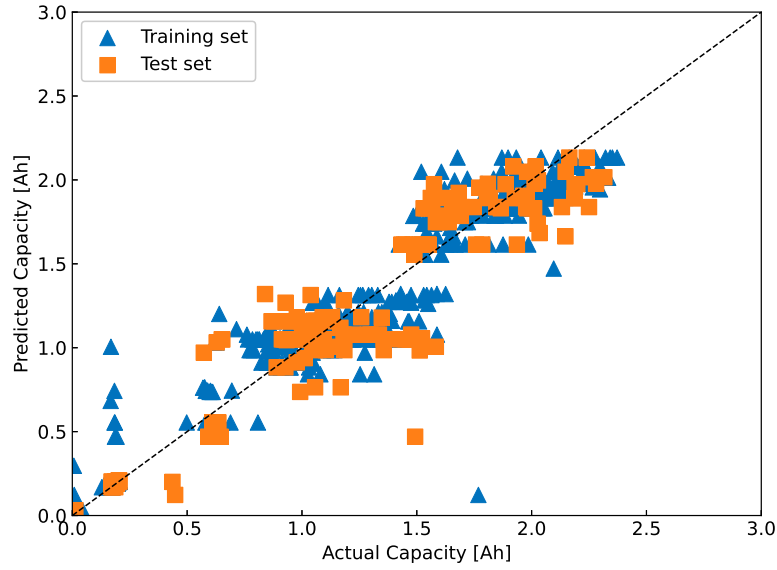


Figure 18: (a) Selection of the BTPF using the Pearson correlation coefficient between each candidate two-point feature and capacities of 157 cells in the training set. F01 to F100 represent 100 relaxation time values between 0 s and 7200 s at intervals of 72 s. The colors are determined based on the Pearson correlation coefficient values. (b) Capacities of 196 cells in Dataset 6 plotted as a function of $DTP_{ADIS:6120s-6984s} \Delta V_{n-1}/t(t)$, with a Pearson correlation coefficient of 0.804.



(a)



(b)

Figure 19: SoH estimation results of different features on 196 cells in Dataset 6. (a) SoH estimation results of $DTP_{ADIS:6120s-6984s} \triangleq V_{n-1}/t(t)$. The input of the XGBoost regression model is $DTP_{ADIS:6120s-6984s} \triangleq V_{n-1}/t(t)$, and the output is the cell capacity. (b) SoH estimation results of statistical features [Var, Ske, Max]. The input of the XGBoost regression model training is statistical features [Var, Ske, Max], and the output is the cell capacity.

$V_{n-1}/t(t)$. Fewer data points mean less data collection, storage, and computing costs.

4.2.5. *Rationalization of diagnostic performance*

Results in [44] and [74] show that EIS curve and its changing trend contain rich information about Li-ion battery aging. In EIS, the high and medium frequency impedance spectrum that represents the solid electrolyte interphase resistance R_{sei} and the charge transfer resistance R_{ct} can be utilized to quantify the LLI, and the low frequency impedance spectrum indicating the diffusion of Li-ions can be utilized to quantify the LAM [74]. Results in [54] and [76] show that the identified multi-timescale information and the changing trend of DRT curves can be utilized to quantify the LLI and LAM in Li-ion batteries. Similar to the raw impedance features and statistical features extracted from EIS [46, 49] and DRT curves [57, 58], we attribute the success of BTPFs extracted from EIS and DRT curves in the diagnosis task to capturing the changing trends of LAM and LLI.

Results in [61, 62] show that relaxation voltage curve and its changing trend can be utilized to characterize the aging modes of Li-ion batteries, such as SEI-driven LLI, Li plating related LLI, and LAM_{PE} . Similar to the raw voltage features and statistical features extracted from relaxation voltage curves [45, 59], we attribute the success of BTPFs extracted from relaxation voltage curves in the diagnosis task to capturing the changing trends of LAM and LLI.

5. Conclusions

Data-driven prognostic and diagnostic methods are promising in accelerating the optimization (including the optimization of design, production, and management) and safer operation of Li-ion batteries. We proposed a BTPF extraction method based on the first principle and conducted comprehensive tests on 820 cells from 6 open source datasets (covering 5 cell chemistries, 7 cell manufacturers, and 3 cell data types). The proposed BTPFs can achieve prognostic and diagnostic accuracy comparable to the SOAT features using only two data points in each cycle. This work well answers an important question that

has been unresolved for data-driven battery prognostic and diagnostic methods: What is the minimum amount of data required to extract features for accurate battery prognosis and diagnosis? The answer given by this work is that two points are enough! The success of BTPFs is rationalized by effectively capturing the changing trends of *LLI* and *LAM* during cell degradation. In general, this work challenges the cognition of existing studies on the difficulty of battery prognosis and diagnosis tasks, subverts the fixed pattern of establishing prognosis and diagnosis methods for complex dynamic systems through deliberate feature engineering, highlights the promise of data-driven methods for field battery prognosis and diagnosis applications, and provides a new benchmark for future studies.

6. Data availability

The Dataset 1 used in this study is an open source dataset published by Severson et al. [25] (124 LFP cells) and Attia et al. [13] (45 LFP cells), and available at <https://data.matrio.io/1>. The Dataset 2 used in this study is an open source dataset published by Li et al. [34] (225 cells) and available at <https://doi.org/10.25380/iastate.22582234>. The Dataset 3 used in this study is an open source dataset published by Jones et al. [46] (88 cells) and available at <https://doi.org/10.5281/zenodo.6645536>. The Dataset 4 used in this study is an open source dataset published by Zhang et al. [49] (12 cells) and available at <https://doi.org/10.5281/zenodo.3633835>. The Dataset 5 used in this study is an open source dataset published by Zhu et al. [45] (130 cells) and available at <https://doi.org/10.5281/zenodo.6379165>. The Dataset 6 used in this study is an open source dataset published by Wildfeuer et al. [22] (196 cells) and available at <https://mediatum.ub.tum.de/1713382>.

7. Code availability

The code used in this study is available at <https://github.com/Zhao-YB/DatasetX>.

8. Acknowledgements

This work is supported by the National Natural Science Foundation of Zhejiang Province (Grant No. LQ23E050013).

9. Author contributions

H.L. conceived the method. H.L., Y.Z., and J.C. conducted the tests. H.L. and Y.Z. developed the best two-point feature extraction method. H.L. and Y.Z. performed the diagnosis and prognosis modeling. H.L., Y.Z., H.Z., Z.D., M.C., X.W., and Z.L performed the data collection, data management, and raw data preprocessing. H.L., Y.Z., X. F., J. L., and J.C. performed the visualization and interpreted the results. H.L., Y.Z., H.Z., and J.C. wrote the original draft. H.L., Y.Z., H.Z., X. F., J. L., and J.C. edited the manuscript. All authors reviewed the manuscript. H.L. and J.C. supervised the work.

10. Competing interests

The authors declare no competing interests.

References

- [1] S. Link, A. Stephan, D. Speth, P. Plötz, Rapidly declining costs of truck batteries and fuel cells enable large-scale road freight electrification, *Nature Energy* (2024) 1–8.
- [2] Z. P. Cano, D. Banham, S. Ye, A. Hintennach, J. Lu, M. Fowler, Z. Chen, Batteries and fuel cells for emerging electric vehicle markets, *Nature Energy* 3 (4) (2018) 279–289.
- [3] R. Schmich, R. Wagner, G. Hörpel, T. Placke, M. Winter, Performance and cost of materials for lithium-based rechargeable automotive batteries, *Nature Energy* 3 (4) (2018) 267–278.
- [4] V. Viswanathan, A. H. Epstein, Y.-M. Chiang, E. Takeuchi, M. Bradley, J. Langford, M. Winter, The challenges and opportunities of battery-powered flight, *Nature Energy* 601 (7894) (2022) 519–525.

- [5] C.-Y. Wang, T. Liu, X.-G. Yang, S. Ge, N. V. Stanley, E. S. Rountree, Y. Leng, B. D. McCarthy, Fast charging of energy-dense lithium-ion batteries, *Nature* 611 (7936) (2022) 485–490.
- [6] J. Janek, W. G. Zeier, Challenges in speeding up solid-state battery development, *Nature Energy* 8 (3) (2023) 230–240.
- [7] C. Gervill  -Mouravieff, W. Bao, D. A. Steingart, Y. S. Meng, Non-destructive characterization techniques for battery performance and life-cycle assessment, *nature reviews electrical engineering* (2024, in press).
- [8] Q. Zhao, S. Stalin, C.-Z. Zhao, L. A. Archer, Designing solid-state electrolytes for safe, energy-dense batteries, *Nature Reviews Materials* 5 (3) (2020) 229–252.
- [9] X. Hu, L. Xu, X. Lin, M. Pecht, Battery lifetime prognostics, *Joule* 4 (2) (2020) 310–346.
- [10] M.-F. Ng, J. Zhao, Q. Yan, G. J. Conduit, Z. W. Seh, Predicting the state of charge and health of batteries using data-driven machine learning, *Nature Machine Intelligence* 2 (3) (2020) 161–170.
- [11] N. H. Paulson, J. Kubal, L. Ward, S. Saxena, W. Lu, S. J. Babinec, Feature engineering for machine learning enabled early prediction of battery lifetime, *Journal of Power Sources* 527 (2022) 231127.
- [12] A. Weng, P. Mohtat, P. M. Attia, V. Sulzer, S. Lee, G. Less, A. Stefanopoulou, Predicting the impact of formation protocols on battery lifetime immediately after manufacturing, *Joule* 5 (11) (2021) 2971–2992.
- [13] P. M. Attia, A. Grover, N. Jin, K. A. Severson, T. M. Markov, Y.-H. Liao, M. H. Chen, B. Cheong, N. Perkins, Z. Yang, P. K. Herring, M. Aykol, S. J. Harris, R. D. Braatz, S. Ermon, W. C. Chueh, Closed-loop optimization of fast-charging protocols for batteries with machine learning, *Nature* 578 (7795) (2020) 397–402.

- [14] Y. Wang, J. Tian, Z. Sun, L. Wang, R. Xu, M. Li, Z. Chen, A comprehensive review of battery modeling and state estimation approaches for advanced battery management systems, *Renewable and Sustainable Energy Reviews* 131 (2022) 110015.
- [15] J. Zhang, Y. Wang, B. Jiang, H. He, S. Huang, C. Wang, Y. Zhang, X. Han, D. Guo, G. He, M. Ouyang, Realistic fault detection of li-ion battery via dynamical deep learning, *Nature Communications* 14 (1) (2023) 5940.
- [16] J. Zhu, W. Xu, M. Knapp, M. S. D. Darma, L. Mereacre, P. Su, W. Hua, X. Liu-Théato, H. Dai, X. Wei, H. Ehrenberg, A method to prolong lithium-ion battery life during the full life cycle, *Cell Reports Physical Science* 4 (7) (2023) 101464.
- [17] G. d. Reis, C. Strange, M. Yadav, S. Li, Lithium-ion battery data and where to find it, *Energy and AI* 5 (2021) 100081.
- [18] A. Geslin, B. v. Vlijmen, X. Cui, A. Bhargava, P. A. Asinger, R. D. Braatz, W. C. Chueh, Selecting the appropriate features in battery lifetime predictions, *Joule* 7 (9) (2023) 1956–1965.
- [19] Z. Huang, L. Sugiarto, Y.-C. Lu, Feature–target pairing in machine learning for battery health diagnosis and prognosis: A critical review, *EcoMat* 5 (6) (2023) e12345.
- [20] Y. Ning, F. Yang, Y. Zhang, Z. Qiang, G. Yin, J. Wang, S. Lou, Bridging multimodal data and battery science with machine learning, *Matter* 7 (6) (2024) 2011–2032.
- [21] B. v. Vlijmen, V. Lam, P. A. Asinger, X. Cui, D. Ganapathi, S. Sun, P. K. Herring, C. B. Gopal, N. Geise, H. D. Deng, H. L. Thaman, S. D. Kang, A. Trewartha, A. Anapolsky, B. D. Storey, W. E. Gent, R. D. Braatz, W. C. Chueh, Interpretable data-driven modeling reveals complexity of battery aging, *ChemRxiv* (2024, in press).
- [22] L. Wildfeuer, A. Karger, D. Aygöl, N. Wassiliadis, A. Jossen, M. Lienkamp, Experimental degradation study of a commercial lithium-ion battery, *Journal of Power Sources* 560 (2023) 232498.

- [23] D. Roman, S. Saxena, V. Robu, M. Pecht, D. Flynn, Machine learning pipeline for battery state-of-health estimation, *Nature Machine Intelligence* 3 (5) (2021) 447–456.
- [24] S. Tao, H. Liu, C. Sun, H. Ji, G. Ji, Z. Han, R. Gao, J. Ma, R. Ma, Y. Chen, S. Fu, Y. Wang, Y. Sun, Y. Rong, X. Zhang, G. Zhou, H. Sun, Collaborative and privacy-preserving retired battery sorting for profitable direct recycling via federated machine learning, *Nature Communications* 14 (1) (2023) 8032.
- [25] K. A. Severson, P. M. Attia, N. Jin, N. Perkins, B. Jiang, Z. Yang, M. H. Chen, M. Aykol, P. K. Herring, D. Fraggedakis, M. Z. Bazant, S. J. Harris, W. C. Chueh, R. D. Braatz, Data-driven prediction of battery cycle life before capacity degradation, *Nature Energy* 4 (5) (2019) 383–391.
- [26] B. Jiang, W. E. Gent, F. Mohr, S. Das, M. D. Berliner, M. Forsuelo, H. Zhao, P. M. Attia, A. Grover, P. K. Herring, M. Z. Bazant, S. J. Harris, S. Ermon, W. C. Chueh, R. D. Braatz, Bayesian learning for rapid prediction of lithium-ion battery-cycling protocols, *Joule* 5 (12) (2021) 3187–3203.
- [27] N. Guo, S. Chen, J. Tao, Y. Liu, J. Wan, X. Li, Semi-supervised learning for explainable few-shot battery lifetime prediction, *Joule* 8 (6) (2024) 1820–1836.
- [28] Q. Wang, Z. Wang, P. Liu, L. Zhang, D. U. Sauer, W. Li, Large-scale field data-based battery aging prediction driven by statistical features and machine learning, *Cell Reports Physical Science* 4 (12) (2023) 101720.
- [29] J. Lu, R. Xiong, J. Tian, C. Wang, F. Sun, Deep learning to estimate lithium-ion battery state of health without additional degradation experiments, *Nature Communications* 14 (1) (2023) 2760.
- [30] F. Wang, Z. Zhai, Z. Zhao, Y. Di, X. Chen, Physics-informed neural network for lithium-ion battery degradation stable modeling and prognosis, *Nature Communications* 15 (1) (2024) 4332.
- [31] M. Dubarry, D. Beck, Analysis of synthetic voltage vs. capacity datasets for big data li-ion diagnosis and prognosis, *Energies* 14 (9) (2021) 2371.

- [32] M. Dubarry, D. Beck, Big data training data for artificial intelligence-based Li-ion diagnosis and prognosis, *Journal of Power Sources* 479 (2020) 228806.
- [33] M. Dubarry, M. Bercibar, A. Devie, D. Anseán, N. Omar, I. Villarreal, State of health battery estimator enabling degradation diagnosis: Model and algorithm description, *Journal of Power Sources* 360 (2017) 59–69.
- [34] T. Li, Z. Zhou, A. Thelen, D. A. Howey, C. Hu, Predicting battery lifetime under varying usage conditions from early aging data, *Cell Reports Physical Science* 5 (4) (2024) 101891.
- [35] P. M. Attia, K. A. Severson, J. D. Witmer, Statistical learning for accurate and interpretable battery lifetime prediction, *Journal of The Electrochemical Society* 168 (2021) 090547.
- [36] L. Zheng, J. Zhu, D. D.-C. Lu, G. Wang, T. He, Incremental capacity analysis and differential voltage analysis based state of charge and capacity estimation for lithium-ion batteries, *Energy* 150 (2018) 759–769.
- [37] C. Weng, Y. Cui, J. Sun, H. Peng, On-board state of health monitoring of lithium-ion batteries using incremental capacity analysis with support vector regression, *Journal of Power Sources* 235 (2013) 36–44.
- [38] X. Li, C. Yuan, X. Li, Z. Wang, State of health estimation for li-ion battery using incremental capacity analysis and gaussian process regression, *Energy* 190 (2020) 116467.
- [39] M. Wei, P. Balaya, M. Ye, Z. Song, Remaining useful life prediction for 18650 sodium-ion batteries based on incremental capacity analysis, *Energy* 261 (2022) 125151.
- [40] F. Xia, K. Wang, J. Chen, State of health and remaining useful life prediction of lithium-ion batteries based on a disturbance-free incremental capacity and differential voltage analysis method, *Journal of Energy Storage* 64 (2023) 107161.

- [41] L. Wang, C. Pan, L. Liu, Y. Cheng, X. Zhao, On-board state of health estimation of LiFePO₄ battery pack through differential voltage analysis, *Applied Energy* 168 (2016) 465–472.
- [42] A. Barai, K. Uddin, M. Dubarry, L. Somerville, A. McGordon, P. Jennings, I. Bloom, A comparison of methodologies for the non-invasive characterisation of commercial Li-ion cells, *Progress in Energy and Combustion Science* 72 (2019) 1–31.
- [43] W. Hu, Y. Peng, Y. Wei, Y. Yang, Application of electrochemical impedance spectroscopy to degradation and aging research of lithium-ion batteries, *Journal of Physical Chemistry C* 127 (9) (2023) 4465—4495.
- [44] P. Iurilli, C. Brivio, V. Wood, On the use of electrochemical impedance spectroscopy to characterize and model the aging phenomena of lithium-ion batteries: a critical review, *Journal of Power Sources* 505 (2021) 229860.
- [45] J. Zhu, Y. Wang, Y. Huang, R. B. Gopaluni, Y. Cao, M. Heere, M. J. Mühlbauer, L. Mereacre, H. Dai, X. Liu, A. Senyshyn, X. Wei, M. Knapp, H. Ehrenberg, Data-driven capacity estimation of commercial lithium-ion batteries from voltage relaxation, *Nature Communications* 13 (1) (2022) 2261.
- [46] P. K. Jones, U. Stimming, A. A. Lee, Impedance-based forecasting of lithium-ion battery performance amid uneven usage, *Nature Communications* 13 (1) (2022) 4806.
- [47] B. Jiang, J. Zhu, X. Wang, X. Wei, W. Shang, H. Dai, A comparative study of different features extracted from electrochemical impedance spectroscopy in state of health estimation for lithium-ion batteries, *Applied Energy* 322 (2022) 119502.
- [48] Y. Zhou, G. Dong, Q. Tan, X. Han, C. Chen, J. Wei, State of health estimation for lithium-ion batteries using geometric impedance spectrum features and recurrent gaussian process regression, *Energy* 262 (2023) 125514.

- [49] Y. Zhang, Q. Tang, Y. Zhang, J. Wang, U. Stimming, A. A. Lee, Identifying degradation patterns of lithium ion batteries from impedance spectroscopy using machine learning, *Nature Communications* 11 (1) (2020) 1706.
- [50] A. Maradesa, B. Py, J. Huang, Y. Lu, P. Iurilli, A. Mrozinski, H. M. Law, Y. Wang, Z. Wang, J. Li, S. Xu, Q. Meyer, J. Liu, C. Brivio, A. Gavriluk, K. Kobayashi, A. Bertei, N. J. Williams, C. Zhao, M. Danzer, M. Zic, P. Wu, V. Yrjänä, S. Pereverzyev, Y. Chen, A. Weber, S. V. Kalinin, J. P. Schmidt, Y. Tsur, B. A. Boukamp, Q. Zhang, M. Gaberšček, R. O'Hayre, C. Francesco, Advancing electrochemical impedance analysis through innovations in the distribution of relaxation times method, *Joule* (2024, in press).
- [51] Y. Zhao, S. Kücher, A. Jossen, Investigation of the diffusion phenomena in lithium-ion batteries with distribution of relaxation times, *Electrochimica Acta* 432 (2022) 141174.
- [52] Q. Zhang, D. Wang, E. Schaltz, D.-I. Stroe, A. Gismero, B. Yang, Degradation mechanism analysis and state-of-health estimation for lithium-ion batteries based on distribution of relaxation times, *Journal of Energy Storage* 55 (2022) 105386.
- [53] R. He, Y. He, W. Xie, B. Guo, S. Yang, Comparative analysis for commercial li-ion batteries degradation using the distribution of relaxation time method based on electrochemical impedance spectroscopy, *Energy* 263 (2023) 125972.
- [54] X. Chen, L. Li, M. Liu, T. Huang, A. Yu, Detection of lithium plating in lithium-ion batteries by distribution of relaxation times, *Journal of Power Sources* 496 (2021) 229867.
- [55] R. Soni, J. B. Robinson, P. R. Shearing, D. J. Brett, A. J. Rettie, T. S. Miller, Lithium-sulfur battery diagnostics through distribution of relaxation times analysis, *Energy Storage Materials* 51 (2022) 97–107.

- [56] M. J. Jung, S.-G. Lee, K.-S. Choi, A new diagnostic indicator for lithium-ion batteries via electrochemical impedance spectroscopy: Harnessing the highest frequency peak in distribution of relaxation times, *Journal of Power Sources* 611 (2024) 234743.
- [57] Y. Zhu, B. Jiang, J. Zhu, X. Wang, R. Wang, X. Wei, H. Dai, Adaptive state of health estimation for lithium-ion batteries using impedance-based timescale information and ensemble learning, *Energy* 284 (2023) 129283.
- [58] Z. Su, J. Lai, J. Su, C. Zhou, Y. Shi, X. Bao, Modeling and health feature extraction method for lithium-ion batteries state of health estimation by distribution of relaxation times, *Journal of Energy Storage* 90 (2024) 111770.
- [59] G. Fan, X. Zhang, Battery capacity estimation using 10-second relaxation voltage and a convolutional neural network, *Applied Energy* 330 (2023) 120308.
- [60] A. Fernando, M. Kuipers, G. Angenendt, K.-P. Kairies, M. Dubarry, Benchmark dataset for the study of the relaxation of commercial NMC-811 and LFP cells, *Cell Reports Physical Science* 5 (1) (2024) 101754.
- [61] B.-R. Chen, C. M. Walker, S. Kim, M. R. Kunz, T. R. Tanim, E. J. Dufek, Battery aging mode identification across NMC compositions and designs using machine learning, *Joule* 6 (12) (2022) 2776–2793.
- [62] B.-R. Chen, M. R. Kunz, T. R. Tanim, E. J. Dufek, A machine learning framework for early detection of lithium plating combining multiple physics-based electrochemical signatures, *Cell Reports Physical Science* 2 (3) (2021) 100352.
- [63] B. Jiang, Y. Zhu, J. Zhu, X. Wei, H. Dai, An adaptive capacity estimation approach for lithium-ion battery using 10-min relaxation voltage within high state of charge range, *Energy* 263 (C) (2023) 125802.

- [64] H. Xiang, Y. Wang, X. Zhang, Z. Chen, Two-level battery health diagnosis using encoder–decoder framework and gaussian mixture ensemble learning based on relaxation voltage, *IEEE Transactions on Transportation Electrification* 10 (2) (2024) 3966–3975.
- [65] K. Qian, B. Huang, A. Ran, Y.-B. He, B. Li, F. Kang, State-of-health (SOH) evaluation on lithium-ion battery by simulating the voltage relaxation curves, *Electrochimica Acta* 303 (2019) 183–191.
- [66] M. Reichert, D. Andre, A. Rösman, P. Janssen, H.-G. Bremes, D. Sauer, S. Passerini, M. Winter, Influence of relaxation time on the lifetime of commercial lithium-ion cells, *Journal of Power Sources* 239 (2013) 45–53.
- [67] V. Sulzer, P. Mohtat, A. Aitio, S. Lee, Y. T. Yeh, F. Steinbacher, M. U. Khan, J. W. Lee, S. J. B., A. G. Stefanopoulou, D. A. Howey, The challenge and opportunity of battery lifetime prediction from field data, *Joule* 5 (8) (2021) 1934–1955.
- [68] V. Steininger, K. Rumpf, P. Hüsön, W. Li, D. U. Sauer, Automated feature extraction to integrate field and laboratory data for aging diagnosis of automotive lithium-ion batteries, *Cell Reports Physical Science* 4 (10) (2023) 101596.
- [69] X. Han, L. Lu, Y. Zheng, X. Feng, Z. Li, J. Li, M. Ouyang, A review on the key issues of the lithium ion battery degradation among the whole life cycle, *ETransportation* 1 (2019) 100005.
- [70] T. Hasegawa, H. Imanishi, M. Nada, Y. Ikogi, Development of the fuel cell system in the Mirai FCV, *SAE Technical Paper 2016-01* (2016) 1185.
- [71] C. Mizutani, M. Shiozawa, T. Maruo, A. Shinji, On-board control system of water content inside FCV stack by electrochemical impedance spectroscopy, *ECS Transactions* 80 (8) (2017) 357–365.
- [72] M. Winter, B. Barnett, K. Xu, Before Li ion batteries, *Chemical reviews* 118 (23) (2018) 11433–11456.

- [73] H. M. Preger, Yuliyaand Barkholtz, A. Fresquez, D. L. Campbell, B. W. Juba, J. Romàn-Kustas, S. R. Ferreira, B. Chalamala, Degradation of commercial lithium-ion cells as a function of chemistry and cycling conditions, *Journal of The Electrochemical Society* 167 (2020) 120532.
- [74] J. Guo, Y. Che, K. Pedersen, D.-I. Stroe, Battery impedance spectrum prediction from partial charging voltage curve by machine learning, *Journal of Energy Chemistry* 79 (2023) 211–221.
- [75] T. H. Wan, S. Mattia, C. Chi, C. Francesco, Influence of the discretization methods on the distribution of relaxation times deconvolution: Implementing radial basis functions with DRTtools, *Electrochimica Acta* 184 (2015) 483–499.
- [76] Y. Lu, C.-Z. Zhao, J.-Q. Huang, Q. Zhang, The timescale identification decoupling complicated kinetic processes in lithium batteries, *Joule* 6 (6) (2022) 1172–1198.